AGU ADVANCING EARTH AND SPACE SCIENCES

Water Resources Research

RESEARCH ARTICLE
10.1029/2025WR041911

# Coupling Neutron and X-Ray Imaging of Fluid Mixing and Precipitation in Rocks: Challenges and Opportunities

**Paiman Shafabakhsh[1], Benoît Cordonnier[1,2], Tanguy Le Borgne[1,3], Joachim Mathiesen[1,4], Gaute Linga[1,5], Anne Pluymakers[6], Anders Kaestner[7], Alessandro Tengattini[8,9,10], and François Renard[1,11]**

[1]The Njord Centre, Departments of Geosciences and Physics, University of Oslo, Oslo, Norway, [2]The European Synchrotron Radiation Facility (ESRF), Grenoble, France, [3]Geosciences Rennes, Université de Rennes 1, Rennes, France, [4]Niels Bohr Institute, University of Copenhagen, Copenhagen, Denmark, [5]PoreLab, Department of Physics, Norwegian University of Science and Technology, Trondheim, Norway, [6]Department of Geoscience and Engineering, Delft University of Technology, Delft, The Netherlands, [7]Laboratory for Neutron Scattering and Imaging, Paul Scherrer Institute, Villigen, Switzerland, [8]Institut Laue-Langevin (ILL), Grenoble, France, [9]University Grenoble Alpes, Grenoble INP, CNRS, 3SR, Grenoble, France, [10]Institut universitaire de France (IUF), Paris, France, [11]Université Grenoble Alpes, Université Savoie Mont Blanc, CNRS, IRD, Université Gustave Eiffel, ISTerre, Grenoble, France

**Key Points:**

- We used coupled 4D neutron and X-ray imaging to study fluid mixing and calcite precipitation in basalt
- Neutron imaging can image the mixing of various aqueous solutions in porous basalt during fluid flow
- Simultaneous X-ray imaging of precipitation is challenging but has potential to detect mixing-induced mineralization

**Supporting Information:**

Supporting Information may be found in the online version of this article.

**Correspondence to:**

P. Shafabakhsh,
paimans@uio.no

**Citation:**

Shafabakhsh, P., Cordonnier, B., Le Borgne, T., Mathiesen, J., Linga, G., Pluymakers, A., et al. (2025). Coupling neutron and X-ray imaging of fluid mixing and precipitation in rocks: Challenges and opportunities. *Water Resources Research*, *61*, e2025WR041911. https://doi.org/10.1029/2025WR041911

Received 8 AUG 2025
Accepted 17 NOV 2025

**Abstract** Solute mixing in rocks plays a central role in a wide range of reactive processes. However, how the complex 3D pore structure of rocks governs mixing rates remains largely unknown. Moreover, some mixing-driven reactions—such as dissolution and precipitation—can modify the pore space, with poorly understood consequences for mixing itself. Recent advances in X-ray imaging techniques have significantly enhanced our ability to visualize the pore-scale rock architecture of rocks and a wide range of fluid processes. However, capturing solute mixing and its impact on chemical reactions—such as mineralization—remains a major challenge. Here, we investigated the potential of coupling time-lapse 3D neutron and X-ray imaging to characterize reactive fluid mixing and subsequent calcium carbonate mineralization in porous basalt. Two flow-through experiments were performed with co-injected $CaCl_2$ and $Na_2CO_3$, leading to precipitation. Neutron imaging tracked fluid mixing, while X-ray imaging distinguished the solid matrix from pore space for fluid analysis. The first experiment showed steady transverse mixing, while a second experiment revealed temporal fluctuations due to trapped air, causing multiphase flow. Neutron images indicated significant fluid mixing driven by these fluctuations. A synchrotron X-ray image post-experiment indicated additional mineral precipitates from long-term diffusive mixing. Despite the promising results, several challenges remain, including resolution limits, temporal synchronization between modalities, and accurate fluid phase segmentation. Overall, our findings highlight both the potential and limitations of integrated neutron and X-ray imaging for studying pore-scale reactive transport and mineralization processes.

**Plain Language Summary** Understanding fluid movement inside rocks is crucial for enhancing $CO_2$ storage and other underground applications. This study used neutron and X-ray imaging to explore how reactive fluids mix in basalt rocks and how this process forms calcium carbonate, aiding long-term carbon storage. We conducted experiments by pumping fluids through basalt samples at varying flow rates and employed advanced imaging to observe the mixing and subsequent calcite precipitation. Neutron imaging tracked fluid movement, while X-ray imaging revealed the pores filled with fluids and calcite. Our findings underscore the challenges and opportunities of using these imaging techniques to study pore-scale mixing and reactive transport, providing a framework for future research on optimizing mineral precipitation processes.

## 1. Introduction

Mixing-driven reactions play a central role in many fundamental and practical applications, such as contaminant transport and remediation in the subsurface (Rolle & Le Borgne, 2019; Steefel, 2018), biogeochemical processes and fluxes in catchments (Bandopadhyay et al., 2018; Bochet et al., 2020; De Vriendt, 2022), and $CO_2$ storage (Dai et al., 2020; Kampman et al., 2014; Wang et al., 2023). Mixing-limited reactions are characterized by a high Damköhler number (*Da*), defined as the ratio of the characteristic solute transport time to that of chemical reactions (Valocchi et al., 2019). For such fast reaction kinetics, mixing enables the dissolved reactants to meet and control the product formation (Cirpka et al., 2006, 2015; Shafabakhsh, Le Borgne, et al., 2024), which occurs at the interface between the segregated reactants (Bauer et al., 2008; Willingham et al., 2008). One such fast reaction

is mineral precipitation, which occurs generally rapidly compared to the transport time scales (Bhandari et al., 2016; Montes-Hernandez et al., 2016). Dissolution/precipitation reactions can then alter pore structures at scales smaller than those typically addressed by continuum models (Noiriel & Soulaine, 2021; Sabo & Beckingham, 2021), leading to various patterns of mineral formation depend on the mixing dynamics at the pore scale (Emmanuel & Berkowitz, 2005).

Reactive transport in porous media is commonly studied through Darcy-scale or field-scale models, focusing on solute dispersion within a framework where continuous media approximation holds (e.g., Aradóttir et al., 2012; Postma et al., 2022). In these models, the pore scale dynamics, which cannot be resolved, are typically approximated by incorporating effective reaction kinetics that are derived from well-mixed conditions (Dentz et al., 2023). Yet, the persistence of incomplete mixing at the pore scale often leads to an overprediction of the rates of mixing-limited reactions (Izumoto et al., 2023; Kang et al., 2019; Sanquer et al., 2024; Valocchi et al., 2019). High-resolution simulations and observations in idealized 2D porous media have shown that the presence of chemical gradients at the pore scale significantly affects mineralization by creating localized areas of precipitation (Deng et al., 2021; Liu et al., 2015), which can, in turn, affect fluid flow and mixing. Several studies have addressed incomplete mixing by incorporating pore-scale concentration variability into continuum formulations (e.g., Anna et al., 2014; Izumoto et al., 2025; Porta et al., 2012; Sole-Mari et al., 2020; Tartakovsky et al., 2008). However, linking these theories to pore scale mixing dynamics and their coupling with precipitation remains a challenge. Furthermore, the interplay between reaction kinetics and transport mechanisms, as porosity and permeability undergo transformation during mineralization, is still under study (Putnis, 2021; Zhao et al., 2023). While mixing and precipitation can be visualized in 2D porous media (e.g., Izumoto et al., 2022), the mixing dynamics in complex 3D porous media such as rocks are fundamentally different (e.g., Boon et al., 2016, 2017; Heyman et al., 2020; Puyguiraud et al., 2021). Hence, there is a need for experimental imaging of mixing and precipitation to bridge the gap between pore-scale processes and Darcy-scale modeling.

Advanced imaging techniques such as neutron and X-ray microtomography allow for a detailed examination of fluid-solid interactions within porous media (Bultreys et al., 2016; Cnudde & Boone, 2013; Cole et al., 2006; Mancini et al., 2020). The high flux available in modern synchrotrons and neutron sources enables dynamic imaging with high spatial resolution (Shafabakhsh, Cordonnier, et al., 2024; Tudisco et al., 2019; Ziesche et al., 2020, 2022). Neutron imaging, with its high sensitivity to hydrogen atoms, enables the visualization of aqueous fluid distribution and phase changes in porous materials due to both scattering and absorption (A. P. Kaestner et al., 2016). This technique has been used in various applications, such as the behavior of fluids in geological formations (Kampman et al., 2014; Shafabakhsh, Cordonnier, et al., 2024), water transport in $CO_2$ electrolysis cells (Disch et al., 2022), transport of contaminants (Cordonnier et al., 2019), and water penetration into reinforced concrete (P. Zhang et al., 2010). In contrast, X-ray imaging provides detailed structural information, allowing the characterization of mineral phases and their spatial distribution within the porous matrix (Haide et al., 2022; Hebert et al., 2015). Because X-rays have a lower attenuation coefficient for water than for the solid matrix, fluids often are visualized using contrasting agents such as iodine (Chen et al., 2021; Scanziani et al., 2020; Wennberg et al., 2009; Zou & Sun, 2020). However, distinguishing between different fluids is challenging, as X-rays interact primarily with matter based on density, which leads to similar attenuation coefficients for most fluids (Coles et al., 1998). Furthermore, the required difference in density between the tracer and the resident fluid, may lead to density-driven flows, potentially largely influencing dispersion, mixing and reaction (Tenchine & Gouze, 2005). Since heavy water and normal water have similar densities, the possibility to use heavy water as a tracer with neutron imaging, makes it an interesting experimental methods to investigate transport processes in rocks. To date, the application of neutron imaging to investigate fluid mixing processes in porous media remains unexplored.

In the present study, we explore the impact of the time-dependent mixing between two reactive solutions, and how this reactive mixing promotes mineralization. By conducting flow-through experiments on basalt core samples, we image the dynamic evolution of fluid distribution under two different flow rates, where the mixing between the fluids ultimately induces mineral precipitation. The results of these experiments provide insights into the implications of fluid mixing leading to mineral precipitation under conditions relevant to subsurface carbon storage.

## 2. Motivation in the Context of Mineral Trapping of $CO_2$ in Basalts

While the presented experimental method is relevant to a large range of applications, the study was initially motivated by $CO_2$ mineral trapping in basalts (Nisbet et al., 2024). In this application, a $CO_2$-rich and low pH fluid flows in the pore space and partly dissolves the rock, liberating divalent cations such as $Ca^{2+}$, $Mg^{2+}$, and $Fe^{2+}$. These cations can combine with dissolved $CO_2$ to precipitate carbonate minerals. However, this process occurs only when the fluid becomes supersaturated with respect to carbonate minerals, in this case, when the pH increases to close to neutral. An important mechanism driving the evolution of pH along flow paths is mixing with the resident fluid, which has a larger pH than the acidic $CO_2$ plume (Menefee et al., 2018). Mineralization may then reduce porosity and clog the pore space (e.g., Dávila et al., 2020; Harrison et al., 2016; Luhmann et al., 2017; Ruiz-Agudo et al., 2017; Tutolo et al., 2015). If the extent of precipitation is significant, it can substantially alter the pore volume and connectivity, with important consequences for fluid mixing, transport dynamics, and long-term storage potential (Menefee et al., 2018; Peuble et al., 2015).

In this regard, basalt rock has gained increasing attention for geological $CO_2$ sequestration due to its high reactivity, abundance of calcium- and magnesium-rich silicate minerals, and ability to promote rapid and permanent carbonation reactions (Oelkers & Gislason, 2023; Oelkers et al., 2008; Tutolo et al., 2015). Unlike sedimentary rocks such as sandstones, basalt facilitates faster mineral trapping of $CO_2$ due to its mineralogy and higher dissolution rates under acidic conditions (Gysi & Stefánsson, 2012; Matter et al., 2007). Additionally, basaltic systems exhibit distinct mixing and precipitation dynamics that depend on fluid-rock interaction patterns and pore structure (Kanakiya et al., 2017; Peuble et al., 2015). Understanding pore-scale mixing in such systems is critical to predicting the spatial distribution and extent of carbonate precipitation (Sun et al., 2023). In this context, one mineral of particular interest is calcite ($CaCO_3$), which plays a significant role in long-term geological storage of $CO_2$ by promoting the formation of stable carbonate minerals in porous rocks (Chang et al., 2017; Xu et al., 2017).

## 3. Methods

Two flow-through experiments were conducted on core samples of basalt rocks sourced from Iceland. These experiments, referred to as "Basalt-ILL" and "Basalt-PSI," were respectively performed at the NeXT station at the Institut Laue-Langevin (ILL) in Grenoble, France, and the ICON beamline of the SINQ neutron spallation source at the Paul Scherrer Institute (PSI) in Villigen, Switzerland. Technical details and instrumentation specifications for these beamlines are described in (A. Kaestner et al., 2011; Tengattini et al., 2020), respectively. The subsequent subsections outline the experimental set-up and procedure employed in both experiments.

### 3.1. Experimental Set-Up and Imaging at ILL and PSI

Figure 1 illustrates the setup of the flow-through experiments. The basalt core samples are cylindrical, each with a diameter of 5 cm and a height of 5 cm, with a pore volume fraction of 0.36. Each core sample was placed inside a surrounding jacket made of fluorinated ethylene propylene (FEP), which is transparent to both neutrons and X-rays. Two porous glass spacers were inserted at the top and bottom extremities of the core sample to better diffuse the fluids. This sample assembly was placed inside core holders made of polytetrafluorethylene (PTFE). Pressurized air, sourced continuously from an air reservoir at 6 bar, filled the space between the jacket and the inner wall of the core holder. This air pressure served to confine the rock, mitigating any potential side flows between the jacket and the sample. The applied confining pressure of approximately 6 bar was selected as a compromise between maintaining a sealed sample environment and ensuring sufficient neutron and X-ray transmission through the imaging cell. This pressure safely confined the rock within the flexible jacket without introducing deformation to the core holder. Although this value is lower than typical in situ pressures for $CO_2$ storage in basalts, it reflects the design limits of the imaging setup rather than an attempt to replicate reservoir conditions. The relatively low pressure does not influence the precipitation reaction during the experiment, which is not strongly pressure-sensitive within this range. The core holders have two inlets for fluid co-flow injection, placed 2.5 cm part at the top of the core holder, and two outlets at the bottom for fluid collection. Atmospheric pressure was maintained at the outlets during flow experiments whereas a flow rate was imposed at each inlet. The core holders were mounted on a rotation stage for microtomography image acquisition utilizing both neutron and X-ray sources available at ILL and PSI. While the stage rotated during tomography acquisition, the inlets and outlets

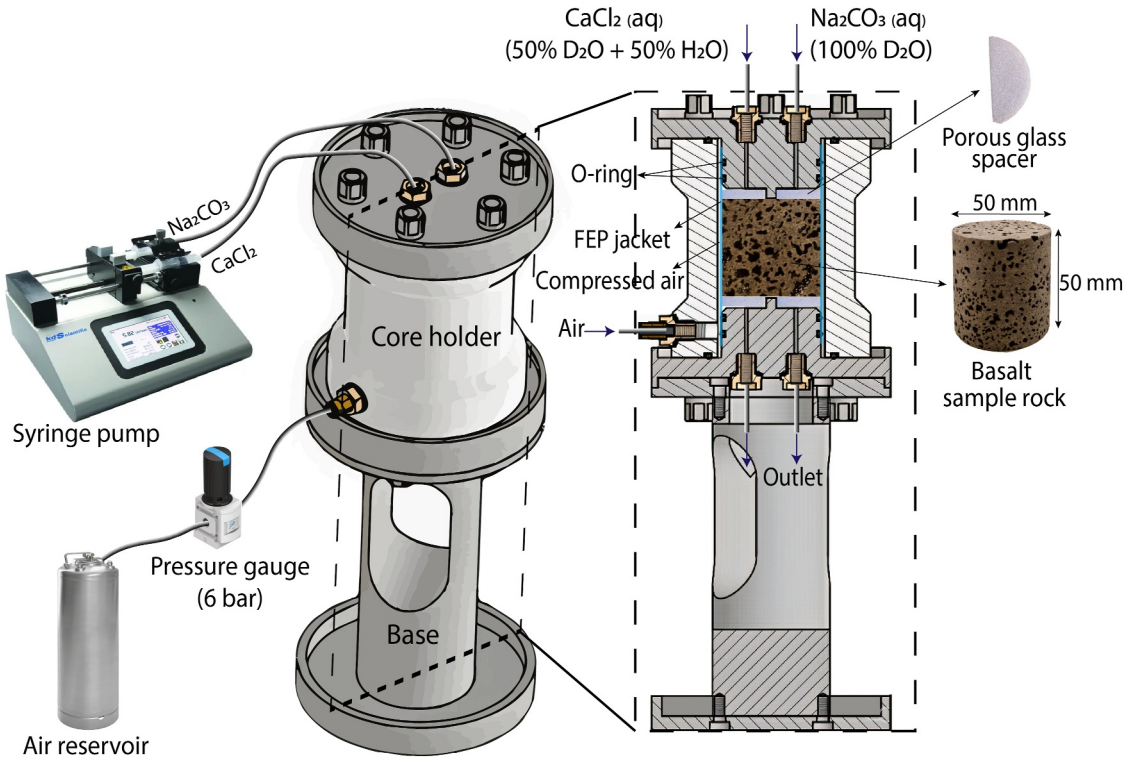


**Figure 1.** Schematic representation of the experimental set-up at the NeXT beamline of the Institut Laue Langevin in France and the ICON beamline of the Paul Scherrer Institute in Switzerland. A basalt core sample (5 cm diameter, 5 cm height) was placed inside the core holder with two inlets for fluid co-flow injection and two outlets. The core sample was enclosed within a fluorinated ethylene propylene (FEP) jacket under a confining air pressure of 6 bar. The core holder was mounted on the rotating stage for image acquisition using both neutron and X-ray sources.

remained fixed within the core holder, which rotated fully. Both experiments were conducted at an ambient temperature of 24°C.

The NeXT beamline at ILL uses a fission-type source. Neutron tomography images of the sample rock were acquired with a voxel size of 84.74 μm, using 800 projections, each the result of the average of three individual projections, over 360-degree rotation, with an average acquisition time of 8 min per scan. The X-ray tomograms obtained at ILL had a voxel size of 35.21 μm, and required 40 min for the acquisition of 1312 projections, each the result of the average of six projections. We also used beamline BM18 at the European Synchrotron Radiation Facility (ESRF) to acquire a high-resolution X-ray image of the entire basalt core sample from the ILL experiment, six months after the injection. Only this sample was imaged at high resolution, as it was already located at ILL in Grenoble, allowing us to transport it easily to ESRF. This high-resolution X-ray tomogram was acquired with a voxel size of 7.06 μm, involving 240,000 projections (16 turns with 15,000 projections each).

For the experiment conducted at PSI, the ICON beamline is a spallation-type source. Time-resolved three-dimensional neutron tomography images of the sample rock at PSI were acquired with a voxel size of 46.12 μm. The neutron tomograms were generated from 626 projections covering a 360-degree rotation of the core holder, with an average acquisition time of 49 min per scan. The X-ray tomograms at PSI had a voxel size of 42.95 μm, requiring 75 min for the acquisition of 1126 projections for one scan.

The acquired image sets at ILL were reconstructed using a parallel algorithm developed at both ILL and the company RX Solutions, France (Tengattini et al., 2020), while the volumes of the projections acquired at PSI were reconstructed using the open-source software MuhRec (A. Kaestner, 2011). The preprocessing steps prior to the reconstructions included scattering correction and spatial median filtering in order to reduce noise. Additionally, the intensity values were normalized using the dark and flat field images, as described in A. Kaestner et al. (2008). Because the neutron and X-ray images had different spatial and temporal resolutions, the X-ray tomograms were acquired before and after the time-lapse neutron sequence for each experiment. The extraction of the pore volume

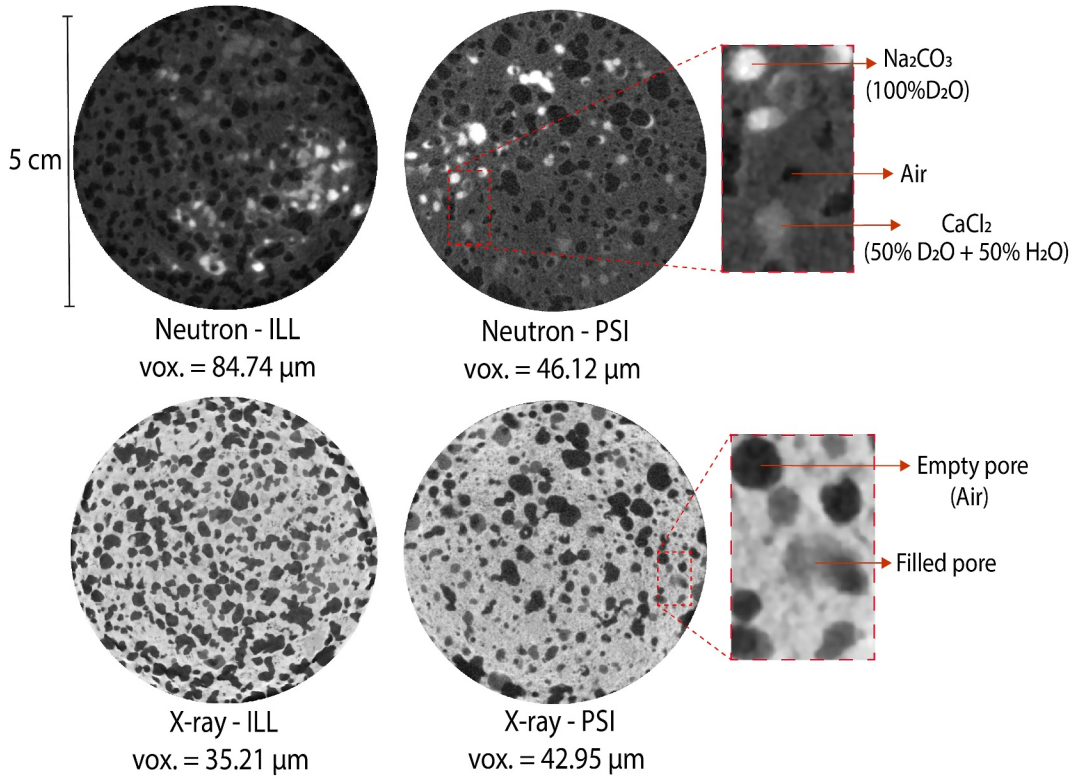


**Figure 2.** Two-dimensional slices of neutron and X-ray tomograms showing horizontal cross-section of basalt rock core samples for the experiments conducted at ILL and PSI. The voxel sizes are indicated for each case. Neutron images allow the separation of the content of the pores, air, and the two different solutions, whereas X-ray images provide a good contrast for the microstructure of the solid.

from the neutron tomograms was based on the high-contrast solid-phase structure captured in the first X-ray scan. The solid matrix of the rock was segmented by applying voxel-based thresholding and subsequently resampling to match the voxel size of the neutron data sets. The segmented X-ray geometry was then registered to the neutron tomograms in a common reference coordinate system using Avizo® software, allowing us to mask the solid phase and isolate the pore volumes filled with air or injected fluids during the time-lapse experiments. The extracted pore volume in the neutron images may have been slightly affected by air dissolving into the injected $D_2O/H_2O$ solutions during the early stages of the experiments. However, this effect is considered negligible relative to the attenuation contrast between the fluids and air in the neutron data.

Figure 2 shows representative horizontal slices of the reconstructed neutron and X-ray tomograms derived from experiments conducted at both ILL and PSI. Neutrons exhibit high sensitivity to hydrogen atoms, allowing for clear contrast between solutions with varying concentrations of these elements. In this case, one salt was dissolved in $D_2O$ (heavy water, with deuterium instead of hydrogen) and the other one was dissolved in a mixture of $H_2O$ (distilled water) and $D_2O$. Consequently, neutron images can be used to differentiate between the two fluids, as illustrated in Figure 2. However, neutrons show a low sensitivity to the basalt matrix, making it difficult to visualize mineral phases or pore structures. To complement this, we used X-ray imaging, which exhibits a considerably lower attenuation coefficient toward hydrogen atoms (and no isotope sensitivity), and is primarily being absorbed by the solid matrix. Therefore, X-rays are more sensitive to changes in material density and provide superior contrast for identifying solid features such as the rock matrix and mineral precipitates. Recent developments such as fast 4D synchrotron X-ray imaging technique (Chen et al., 2021) have advanced the ability to visualize solute dispersion at high temporal and spatial resolutions. Nonetheless, X-ray imaging alone struggles to distinguish between coexisting solutions and evolving solid components as the attenuation values of different fluids and mineral phases can overlap. While X-ray imaging can detect fluids such as water, the contrast is much lower compared to neutrons, making it more challenging to distinguish between different fluids. Combining these

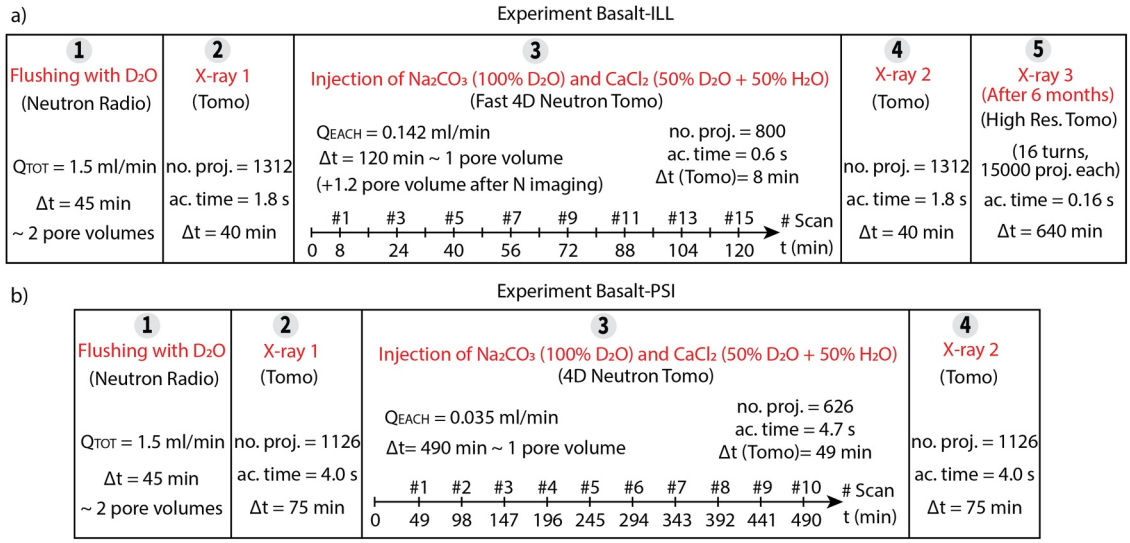


**Figure 3.** The steps of imaging and fluid injections for the two experiments (a) Basalt-ILL and (b) Basalt-PSI. Initially, both core samples were imaged with two-dimensional neutron radiographs during flushing with $D_2O$. The X-ray tomograms (X-ray 1 and X-ray 2) were acquired before and after calcium carbonate precipitation. The precipitation was induced by co-flow injection of $CaCl_2$ and $Na_2CO_3$ solutions while the core samples were imaged with time-lapse three-dimensional neutron tomography. For experiment Basalt-ILL, a high-resolution X-ray scan (X-ray 3) was acquired at ESRF 6 months after the experiment. We also provide the flow rate of the injection (Q), duration of each step ($\Delta t$), number of projections for each tomogram (no. proj.), and average acquisition time (ac. time).

two techniques allows us to capture the dynamic evolution of fluids by neutron imaging and to resolve static structural features of the rock by X-ray imaging.

### 3.2. Reactive Mixing Experiments

The two experiments, Basalt-ILL and Basalt-PSI, were conducted to investigate transient reactive mixing and the resulting precipitation in basalt rocks, using two different facilities with distinct imaging capabilities and experimental constraints. Different flow rates where employed, corresponding totwo Péclet numbers (*Pe*) governing fluid transport in the cores. Calcium carbonate precipitation occurred through the continuous injection of two aqueous solutions containing $CaCl_2$ and $Na_2CO_3$ through the reaction:

$$CaCl_2(aq) + Na_2CO_3(aq) \longrightarrow CaCO_3(s) + 2NaCl(aq). \quad (1)$$

The steps of the experiments Basalt-ILL and Basalt-PSI are summarized in Figure 3. For both cases, an attempt was made to flush the initially dry samples by injecting $D_2O$ with a flow rate of 1.5 mL $min^{-1}$. Our initial objective was to achieve complete saturation of the samples to ensure a single-phase fluid for subsequent flow injections. Despite flushing with $D_2O$, full saturation of the basalt samples could not be achieved. This incomplete saturation resulted from two main factors: (a) a portion of the pore network was isolated and therefore not connected to the main flow system, and (b) some connected pores were bypassed because they were not located along the dominant flow paths. After continuous injection of $D_2O$, no additional changes were observed in the neutron images, indicating that the saturation level had reached its maximum attainable value under the applied conditions. Following this, we acquired X-ray images of the samples. Subsequently, solutions with 1 M of $CaCl_2$ (aq) and 1 M of $Na_2CO_3$ (aq) were continuously injected in parallel from the co-flow inlets, each inlet maintaining a flow rate of 0.142 mL $min^{-1}$ at ILL and 0.035 mL $min^{-1}$ at PSI. These flow rates were determined to ensure the flow through of at least one pore volume in the core sample within a time frame adequate for the acquisition of 15 scans of neutron images at ILL and 10 scans at PSI. Finally, a second round of X-ray images of the samples was acquired after calcite precipitation. After neutron imaging was completed for the Basalt-ILL experiment, the fluid injection continued for approximately 1.2 additional pore volumes at the same flow rate while the setup for the second X-ray imaging was being prepared. Moreover, a third X-ray tomogram of the sample rock was acquired at ESRF with higher resolution after the sample had dried for a period of 6 months. For the experiment Basalt-PSI, logistical constraints prevented high-resolution X-ray imaging of the sample.

The 1 M $CaCl_2$ solution was prepared using a combination of 50% $D_2O$ and 50% $H_2O$, whereas the 1 M $Na_2CO_3$ solution was prepared in 100% $D_2O$. The proportions of $D_2O$ and $H_2O$ for the $CaCl_2$ solution were chosen to optimize the contrast for neutron imaging (Cordonnier et al., 2019; Shafabakhsh, Cordonnier, et al., 2024).

### 3.3. Quantification of Mixing

We performed the experiments at two different flow rates as detailed in Section 3.2. For a flow with average velocity $U$, considering $\tau_a = d/U$ the characteristic advection time over a pore of diameter ($d$), and considering $\tau_d = d^2/D$ the characteristic diffusion time, where $D$ is the diffusion coefficient, the Péclet number ($Pe$) can be defined as

$$Pe = \frac{\tau_d}{\tau_a} = \frac{Ud}{D}. \tag{2}$$

Since mixing occurs at the pore scale, we use the pore diameter as the characteristic length to define advection and diffusion timescales. The average pore diameter of the basalt samples is $d = 1.0$ mm. Despite differences in pore structure, the porosity values are nearly identical (36.8% for Basalt-ILL and 35.9% for Basalt-PSI), which justifies the use of a single representative pore diameter for both samples. The average diffusion coefficient is $D = 9.4 \times 10^{-10}$ $m^2\,s^{-1}$, which is calculated by averaging the diffusion coefficients of solutions $CaCl_2$ and $Na_2CO_3$ (Leaist & Noulty, 1985; Ribeiro et al., 2008). The average flow velocity, derived from the total flow rate divided by the average pore cross-sectional area, is $U = 6.69 \times 10^{-6}$ $m\,s^{-1}$ for experiment Basalt-ILL and $U = 1.65 \times 10^{-6}$ $m\,s^{-1}$ for experiment Basalt-PSI. As a result, the Péclet numbers are $Pe = 7.1$ and $Pe = 1.7$ for the respective experiments. The reaction between $CaCl_2$ and $Na_2CO_3$ can have spatial and temporal variability in the characteristic reaction time; however, a value $\tau_r = 5$ s is reported in a flowing millifluidic experiment of calcite formation (Izumoto et al., 2022). While this value may depend on local flow conditions and system scale, it provides an estimate for reaction time under dynamic mixing. Thus, estimations of the Damköhler number ($Da = \tau_a/\tau_r$) are $Da = 30$ for experiment Basalt-ILL and $Da = 121$ for experiment Basalt-PSI.

To extract the injected fluids from time-lapse neutron tomograms, we utilized the sharp solid-phase distributions from the first X-ray images for each experiment. The solid phase of the rocks was segmented by classifying and labeling voxels of the X-ray image through a thresholding algorithm. This process began with automated global thresholding based on the histogram of voxel intensities to separate the solid matrix from the pore space using Avizo® software. This was followed by a manual correction to improve accuracy in regions where different phases exhibited similar intensity values or imaging artifacts were present. This segmented geometry was then transformed to match the spatial resolution of the neutron images. By registering the segmented solid phase from X-ray to the neutron data sets in a common reference coordinate system with Avizo® software, we were able to mask the solid and extract the pore volumes filled with air or injected fluids from the time-lapse neutron scans. Subsequently, we segmented the two fluids (one consisting of a $D_2O$ solution and the other a mixture of 50% $D_2O$ and 50% $H_2O$) as well as the empty pores in each three-dimensional image, using a thresholding algorithm on the neutron images. The segmentation procedure is limited by the distribution of the voxel intensity and the degree of interplay or separation between the different fluids and phases. Noise and artifacts inherent to the acquisition process, along with potential partial volume effects, also impact segmentation accuracy. A three-dimensional median filter was applied to the neutron images before the segmentation to reduce noise and allow a better separation of the two fluids and air. Segmentation of neutron images was also carried out using Avizo® software with a semi-automatic approach, involving initial automated thresholding combined with user input to correct misclassifications.

While segmentation facilitates qualitative analysis of the two fluids, it may result in an oversimplification of the fluid distribution and does not provide information regarding the *mixing* of these fluids. To quantify fluid mixing within the basalt samples, we employed a statistical approach based on the variance and mean of the concentration of extracted fluids, scaled between 0 and 1 after removing noise outliers. The fluids were extracted from the entire three-dimensional sample volume at each time step. This analysis provides insights into the spatial distribution and homogeneity of fluid mixing within the porous media. We calculated the variance of the concentration of the extracted fluids for each time-lapse neutron image. The mean concentration provides an average measure of the fluid distribution throughout the sample. The variance is related to the spread of concentration values around the

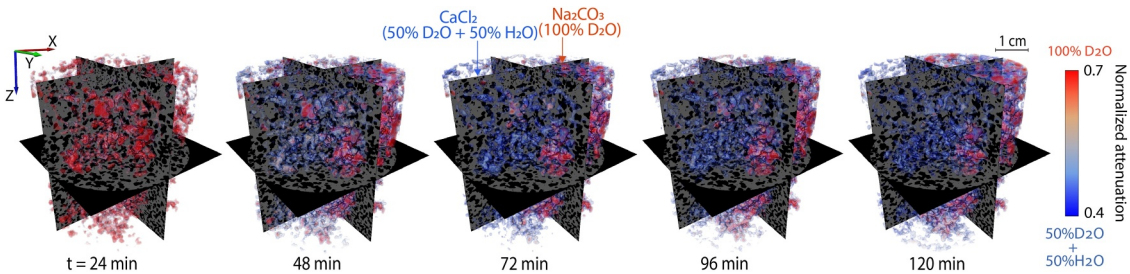


**Figure 4.** Time series of a selection of neutron tomograms acquired during the co-flow injection of $CaCl_2$ in a solution of 50% $D_2O$ + 50% $H_2O$ (blue color) and $Na_2CO_3$ in a solution of 100% $D_2O$ (red color) for the experiment Basalt-ILL.

mean, indicating the degree of heterogeneity in the fluid distribution (Danckwerts, 1952). The variance of concentration $c$ is computed as

$$\sigma^2 = \overline{c^2} - (\overline{c})^2. \tag{3}$$

A higher value of variance indicates greater variability in concentration, indicating a less mixed state of the plume. In contrast, a value close to zero indicates limited spatial heterogeneity in the distribution of different fluids.

## 4. Results

### 4.1. Experiment Basalt-ILL

#### 4.1.1. 4D Neutron Imaging of Fluid Mixing

The Basalt-ILL experiment was carried out with a scan duration of 8 min, allowing a higher flow rate ($Pe = 7.1$). Initially, the rock was flushed with $D_2O$, and most of the connected pores were filled with water. Figure 4 displays a selected series of neutron tomograms from this experiment, showing the co-flow of $CaCl_2$ (solution with 50% $D_2O$ and 50% $H_2O$) and $Na_2CO_3$ (solution with 100% $D_2O$). The images illustrate the transverse mixing of the two fluids throughout the injection. As the co-flow injection proceeds, the small amount of remaining connected empty pores gradually fills with the injected fluids.

We extracted the pore volumes filled with air or injected fluids from the neutron tomograms after masking the solid phase using the initial X-ray image. This step was followed by the segmentation of the two fluids (100% $D_2O$ and 50% $D_2O$ + 50% $H_2O$) and of the empty pores from the time-lapse neutron images. The linear attenuation coefficients of the extracted fluids from neutron tomograms were then scaled between 0 and 1, using the maximum and minimum values (after removing noise outliers). Due to overlap in neutron attenuation properties and partial volume effects, the voxel intensities associated with different fluid mixtures ($D_2O$ vs. 50% $D_2O$ + 50% $H_2O$) are spread around the average values. In the corresponding histograms (Figure 5a) the peak at $c = 0$ corresponds to the average attenuation of the solution 50% $D_2O$ + 50% $H_2O$, while the peak at 0.3 corresponds to the average attenuation of the 100% $D_2O$ solution.

Figure 5a presents the probability density function of the fluid concentrations in the whole sample. As a reference, the distribution from the initial scan ($t = 8$ min) is overlaid in red on each panel to highlight the evolution of concentration distributions over time. Initially, the histogram shows a concentration peak at higher values, indicating the prevalence of $D_2O$ in the pore spaces. As the co-injection progresses, the peak shifts and broadens toward lower concentrations, indicating an increasing presence of the 50% $D_2O$ + 50% $H_2O$ solution, mixing with the $D_2O$ solution. At the final scan ($t = 120$ min), the histogram still exhibits a peak corresponding to $D_2O$, indicating that the fluids flow in parallel in the pore space and mix transversely. Figures 5b and 5c display horizontal slices of the neutron tomograms and the corresponding segmented images from the center of the basalt sample. The segmentation into the two fluids, the pores consistently filled with air, and the solid phase are also depicted for different heights of the sample in the Figures S1 and S2 of Supporting Information S1. The data initially show a higher proportion of $D_2O$ within the pores. Over time, the 50% $D_2O$ + 50% $H_2O$ solution increasingly occupies the pore space. The segmented regions of consistently air-filled pores, indicated in yellow, largely encompass the existing empty pores. Figure 5 also provides the percentage of empty pores relative to the

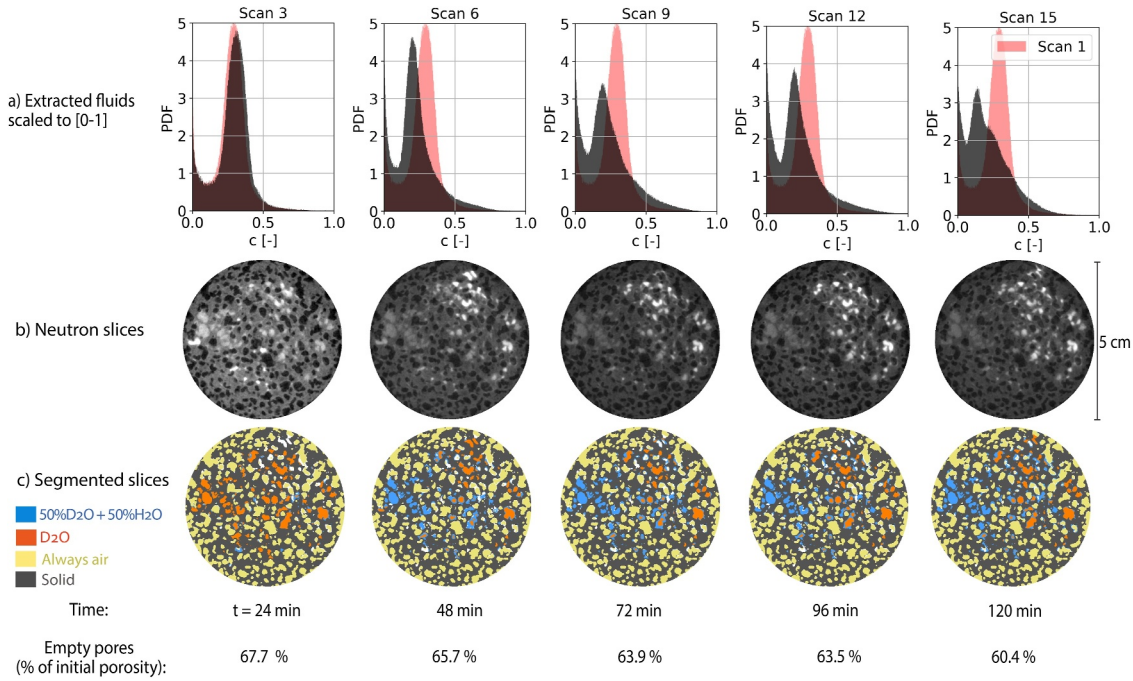


**Figure 5.** (a) Probability density function of the concentration of the fluids extracted from neutron tomograms for the Basalt-ILL experiment. The initial reference distribution from scan 1 ($t = 8$ min) is overlaid in red on each histogram. (b) Two-dimensional slices of neutron scans at the center of the core sample at different times. (c) Segmentation of the corresponding slices into the two fluids, the empty pores that are consistently filled with air, and the solid phase. We also show the percentage of empty pores at each time step with respect to the original porosity.

initial porosity at each time step. This observation suggests that the extent of multiphase flow was limited implying that most of the connected pores were initially saturated. However, a small amount of air still migrated through the pores, resulting in a minor degree of multiphase flow.

Based on the segmentation of the neutron tomograms of the Basalt-ILL experiment, Figure 6 illustrates the distribution of the two fluids and the empty pores along the height of the core sample at various times. The fraction of 100% $D_2O$ across the sample height, as shown in Figure 6a, exhibits a decreasing trend at the beginning (after $t = 24$ min) as this solution was replaced by the solution with 50% $D_2O$ + 50% $H_2O$. This replacement is further supported in Figure 6b, where the proportion of the 50% $D_2O$ + 50% $H_2O$ fluid increases at the same time, indicating its progressive infiltration into the pore spaces of the rock during the early stages of co-injection. Figure 6c shows that the fraction of air-filled pores remained relatively constant, with only a slight decrease, suggesting that the fluids predominantly occupied spaces that were already filled, resulting in minimal multiphase flow. Figure 6d presents the percentage of each fluid within the total fluid-filled pore space over time. Until the third scan ($t = 24$ min), the 50% $D_2O$ + 50% $H_2O$ solution had not fully penetrated the rock, as it was still filling the spacers above the sample. After this point, the transport time required for the second fluid to flow through the rock and replace some of the 100% $D_2O$ solution was approximately three scans (up to $t = 48$ min), after which the fractions of both fluids stabilized. Figure 6e shows a steady decrease in the percentage of empty pores with respect to the original porosity of 36.8%. The small change in the fraction of empty pores during the co-flow injection, approximately 9% of initial porosity throughout the entire process, further confirms the limited occurrence of multiphase flow in this experiment.

To analyze the extent of mixing between the two fluids, we use the scaled attenuation coefficients of the extracted fluids from neutron tomograms as a proxy for the concentration field. Figure 7a shows the mean concentration measured over the whole sample as a function of time, along with the variance of concentration, $\sigma^2$. In the first three scans (until $t = 24$ min), the second fluid was in the upstream chamber and had not yet reached the sample, which explains the stability in the mean concentration. The mean concentration began to drop after this period, and by $t = 48$ min, the pores were increasingly occupied by the solution 50% $D_2O$ + 50% $H_2O$. The variance $\sigma^2$ increased gradually after $t = 24$ min, indicating a greater presence of the second fluid within the rock and an

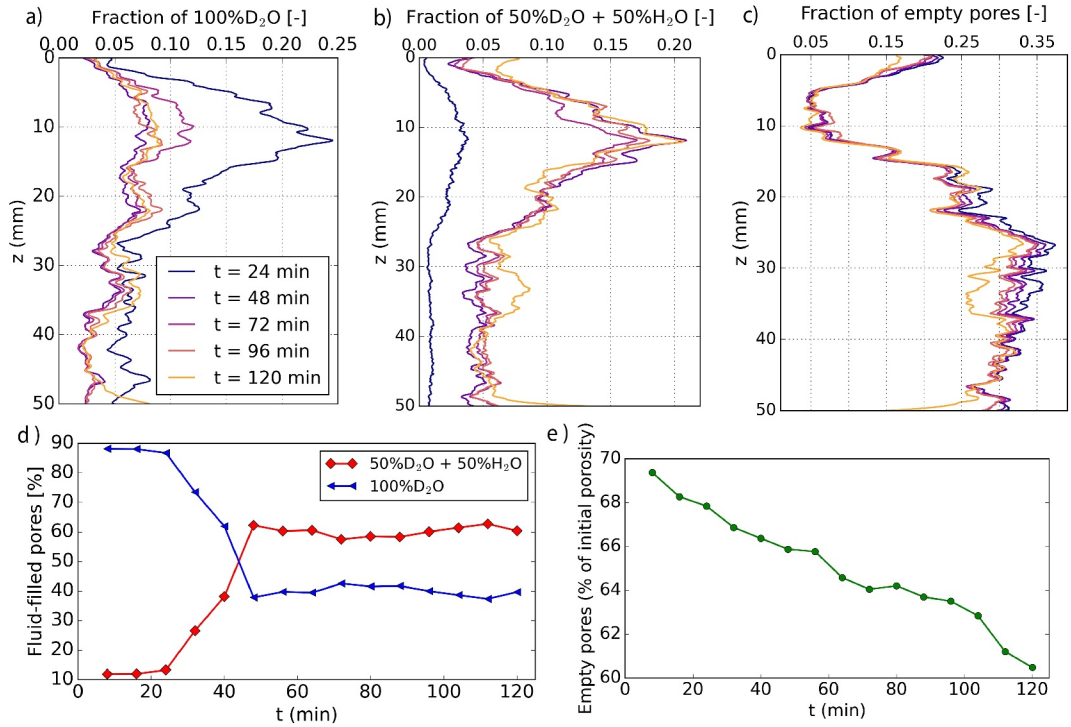


**Figure 6.** Segmentation analysis of neutron tomograms from experiment Basalt-ILL, illustrating the fraction of fluid 100% $D_2O$ (a), fluid 50% $D_2O$ + 50% $H_2O$ (b), and empty pores (c) as a function of height at different time points. Panel (d) presents the relative distribution of each fluid within the total fluid-filled pore volume over time, expressed as a percentage. Panel (e) shows the percentage of empty pore volume with respect to the initial porosity (36.8%), indicating progressive pore filling throughout the experiment.

increase in the spread of concentration values around the mean. The oscillations in both the mean concentration and $\sigma^2$ upon reaching steady-state are minimal, which can be attributed to a limited displacement of pre-existing fluid or air by the injected fluids. After $t = 96$ min, a slight decrease in $\sigma^2$ was observed, indicating more effective mixing and consequently lower variability in concentration. Figures 7b and 7c show the variance and mean concentration through the height of the core sample, at different time points. The variance of concentration through height (Figure 7b) at $t = 24$ min reflects the baseline single-fluid condition, arising from structural heterogeneity of the basalt. A reduction in variance relative to this baseline, observed after the second fluid entered the core ($t \geq 32$ min), indicates progressive homogenization of concentration due to mixing within the pore space. The mean concentration profile through height (Figure 7c) shows a slight variation along the height of the sample, remaining within the same order of magnitude. This result suggests that a steady mixing front was established through the rock.

### 4.1.2. X-Ray Imaging of Filled Pores at ILL and ESRF

X-ray tomography scans for the Basalt-ILL experiment were acquired at three stages: one before (X-ray 1) and one after (X-ray 2) calcite precipitation during the experiment at ILL, and a third, higher-resolution, scan (X-ray 3) at ESRF, conducted after the sample had dried for 6 months, the time required for radioactivity to decay sufficiently. Before acquiring the X-ray 2 scan, fluid injection was continued for approximately 1.2 additional pore volumes at the same flow rate following the completion of neutron imaging, while the imaging setup was being reconfigured. During the imaging of the X-ray 1 and X-ray 2 scans, the pumps were stopped and no fluid was actively injected. However, due to the atmospheric pressure in the outlet tubes of the core holder, some fluid movement driven by gravity likely occurred. This fluid redistribution during X-ray acquisition resulted in some pores appearing filled in X-ray 2 that were empty in the earlier neutron scans, suggesting changes in pore occupancy occurred between the two imaging sessions. For example, Figure S6 in Supporting Information S1 shows some pores that are empty in the neutron image but filled with a solution in the X-ray 2 image. As a result, a direct

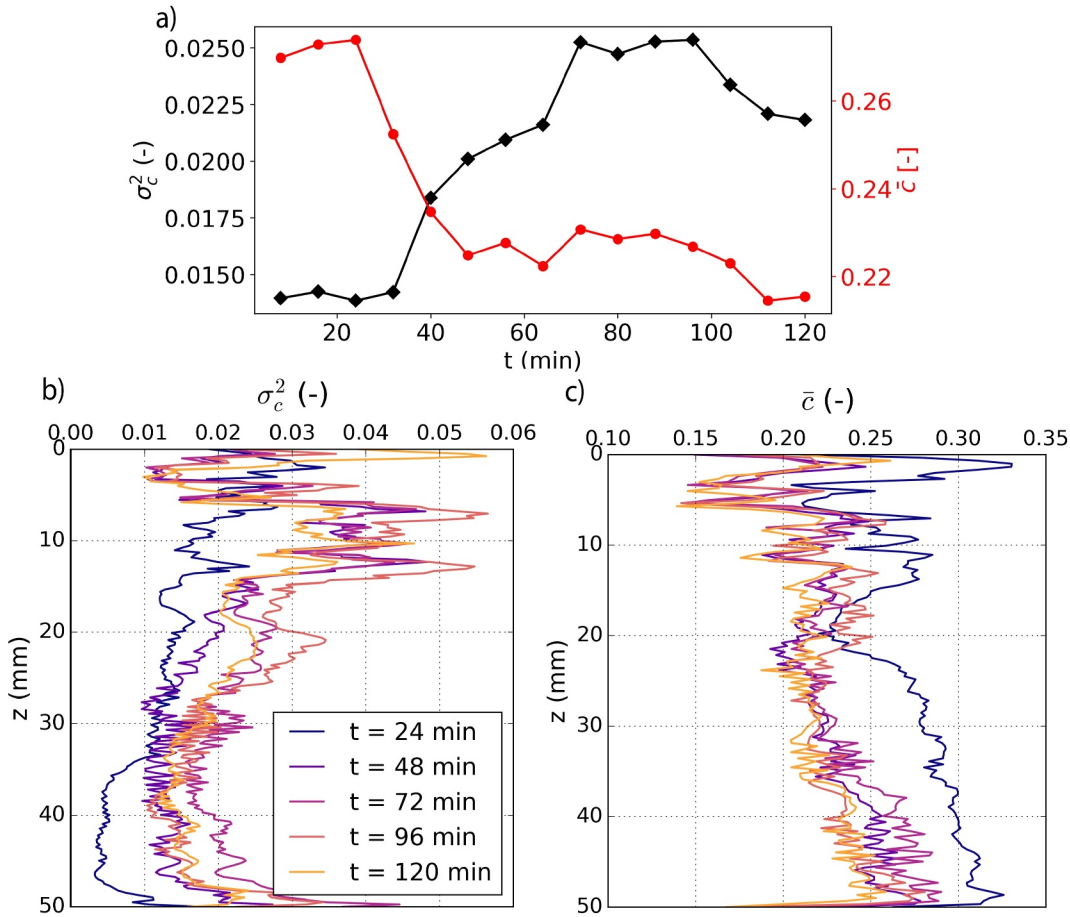


**Figure 7.** (a) The mean concentration of the extracted fluids (red curve with the axis on the right) and the concentration variance (black curve with the axis on the left) through time for the experiment Basalt-ILL. These values were calculated for the entire 3D sample volume, based on the scaled attenuation coefficient extracted from segmented regions containing fluids in the neutron images. The variations of (b) variance and (c) mean concentration through height are shown at different times.

comparison between the fluid detected in the X-ray images and the neutron data is not straightforward. Nevertheless, the comparison between X-ray 1 and X-ray 2 remains useful for identifying regions where pore filling occurred following the post-injection period.

Figure 8a displays two-dimensional slices of the basalt core, oriented perpendicular to the core axis at different heights for the X-ray 1 and X-ray 2 scans. The comparison of the slices from X-ray 1 and X-ray 2 indicates that some pores have been filled, although X-ray tomography data does not allow one to clearly distinguish between the fluids and precipitated calcite, which show overlapping adsorption properties. Figure 8b shows the normalized differences between corresponding slices at different heights, highlighting the changes in pore filling after reactive mixing, either with fluids or precipitates. Figure 8c presents two-dimensional slices at the same heights from a high-resolution X-ray 3 scan of the dried sample, providing a more detailed view of the precipitates within the pores, depicted in blue. Given that the rock was dried before this scan, all segmented areas represent calcite precipitates, along with some potential salt precipitates, which may have formed due to the evaporation of residual fluids during the 6 months after the injection. However, it is important to note that during the injection, we expect only calcite to have precipitated in the rock due to the high solubility of the other salt (NaCl) under the experimental conditions. While this interpretation is based on the known chemistry of the injected solutions, we acknowledge that the presence of minor NaCl residues, even if unlikely, cannot be fully excluded without direct mineralogical analysis. The zoomed-in insets in the figure further reveal the precipitates, which appear in light gray within the pores, while the empty pores appear in black. The precipitation is observed throughout the rock, predominantly along the pore walls. Given the long period that the rock had remained steady prior to this X-ray

10.1029/2025WR041911

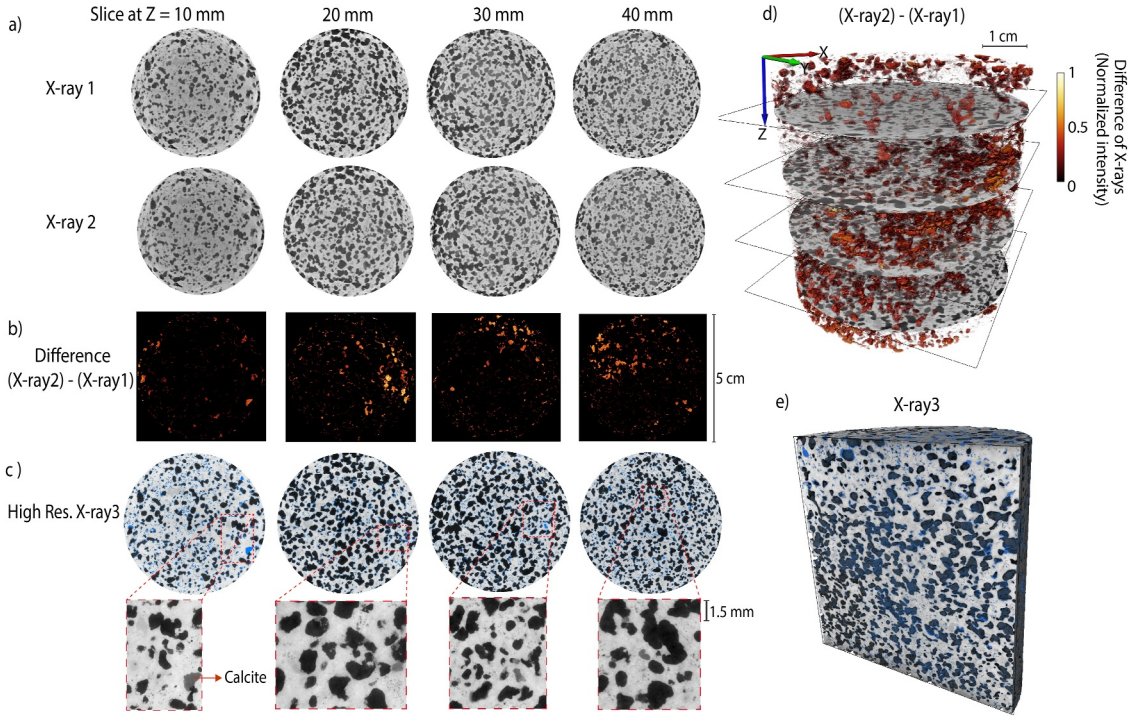


**Figure 8.** X-rays images of experiment Basalt-ILL: (a) Horizontal slices, perpendicular to the core axis at different heights before (X-ray 1) and after (X-ray 2) precipitation acquired at ILL with a voxel size of 35.21 μm. (b) The difference between tomograms X-ray 1 and X-ray 2 for the corresponding slices at different heights. (c) Corresponding two-dimensional slices from high-resolution tomogram X-ray 3 acquired at ESRF after 6 months (with the sample rock dried) with a voxel size of 7.06 μm, including zoomed-in images of small regions where empty pores appear in black. The segmented domains in blue in the full picture show the precipitation. (d) Volume rendering of the difference between X-ray 1 and X-ray 2. (e) Cutaway rendering of the volume of X-ray 3, highlighting the segmented areas of precipitates with a blue color.

scan, it is likely that the precipitation occurred through diffusive mixing after the experiment. Figure 8d provides a three-dimensional rendering of the difference between the X-ray 1 and X-ray 2 scans, visually representing the extent of the pores filled by both fluids and precipitates. Figure 8e shows a cutaway rendering of the volume from the X-ray 3 scan, emphasizing the segmented domains of the precipitation.

The rock used in the Basalt-ILL experiment exhibits a distinct geometric characteristic, with porosity at the top of the rock being lower than in other regions, as shown by comparing the porosity distribution in the slice located at $Z = 10$ mm with the slices at other heights, as shown in Figure 8a. This variation is further confirmed by the porosity distribution profile along the core sample axis, calculated by dividing the total segmented pore volume by the slice surface area in X-ray 1 as shown in Figure 9a. This lower porosity at the top likely reduced local permeability and diverted flow toward more permeable regions, enhancing heterogeneity in fluid transport and promoting localized mixing in certain regions. As the precipitates during the experiment are unconsolidated and not fully solidified, the segmented pore volumes in the X-ray 1 and X-ray 2 scans appear identical, leading to overlapping porosity distributions as shown in Figure 9a. The profile in Figure 9b is derived from the segmentation of the differences between X-ray 2 and X-ray 1 scans, indicating the proportion of pores filled with fluids and calcite precipitates during the experiment. Figure 9c represents the fraction of segmented precipitates from the high-resolution X-ray 3 scan of the dried sample, illustrating the distribution of precipitates (calcite along with potential NaCl) that have formed during the 6-month evaporation period within the pores. Given the additional diffusive mixing between the two solutions after the experiment, which led to more extensive calcite precipitation within the pores of the core sample, it is expected that the sample contains a greater amount of calcite precipitates at the time of the X-ray 3 scan compared to the X-ray 2 scan. While Figures 9b and 9c represent distinct stages and measurement conditions, their indirect comparison provides useful qualitative insights into the spatial evolution of pore filling and mineralization.

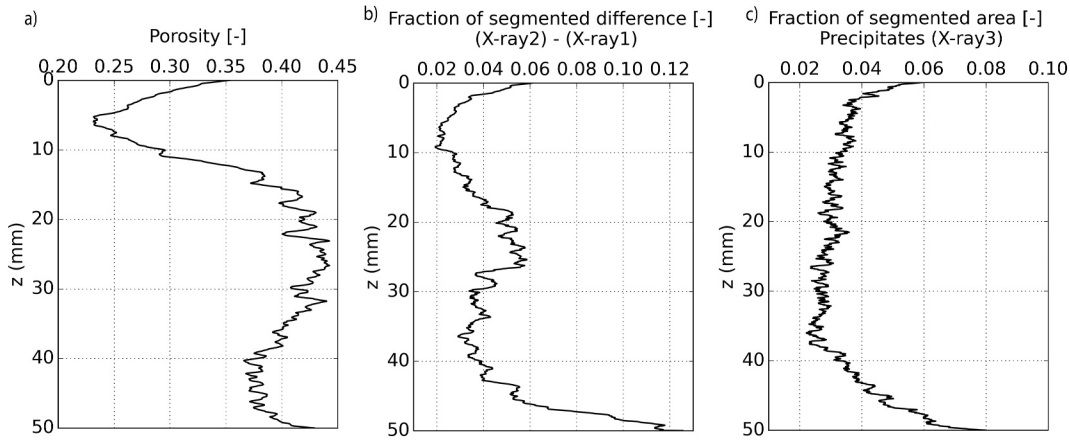


**Figure 9.** (a) Porosity distribution profile along the core sample axis for the Basalt-ILL experiment. (b) Profile illustrating the fraction of segmented differences between tomograms X-ray 2 and X-ray 1. (c) The fraction of segmented precipitation from the high-resolution X-ray 3 scan of the dried sample rock.

It is important to note that the higher density of precipitates observed near the inlet and outlet of the sample is likely related to boundary effects arising from the experimental setup. Although the porous glass spacers at the inlet and outlet were used to maintain uniform flow at both ends of the core, small gaps between the spacers and the rock surface may have allowed limited fluid mixing outside the sample rock. These gaps may have created zones of fluid accumulation, promoting localized clogging and precipitation near the sample boundaries.

### 4.1.3. Calcite Precipitation Induced by Transverse Mixing

Figure 10 presents the mean phase density obtained by averaging the segmented phases over 580 slices for the final neutron tomogram and 6962 slices for high-resolution X-ray 3 tomogram along the height of the Basalt-ILL

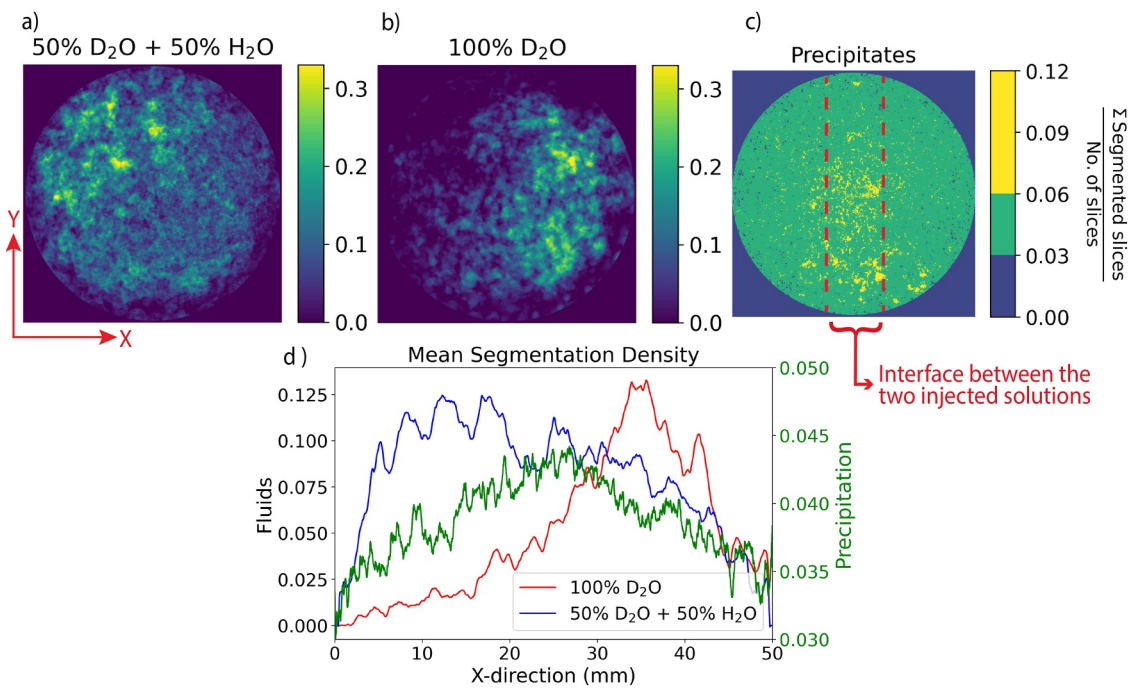


**Figure 10.** Mean segmentation density analysis of fluid mixing and precipitation in the Basalt-ILL experiment. (a) Average of segmented 50% $D_2O$ + 50% $H_2O$ fluid extracted from the last neutron tomogram. (b) Average of segmented 100% $D_2O$ fluid from the last neutron tomogram. (c) Average of segmented precipitation from the high-resolution X-ray 3 scan after drying. (d) Segmentation density profile along the *X*-direction, showing a higher density of precipitates near the interface between the two injected solutions.

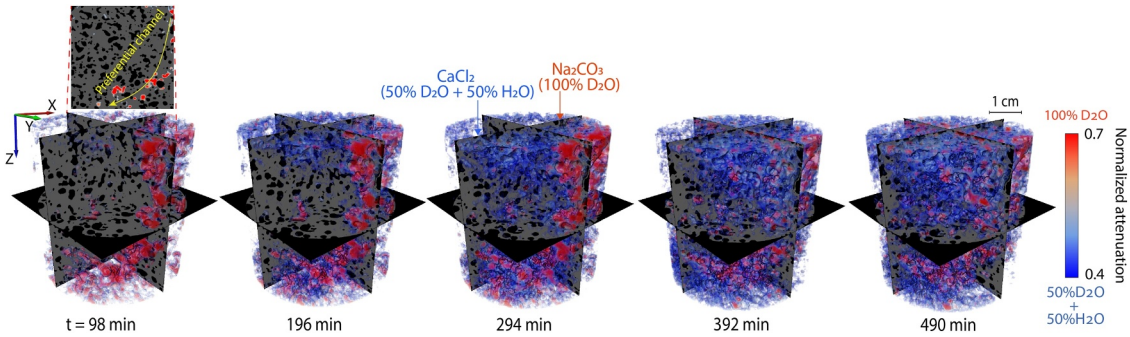


**Figure 11.** Time series of neutron tomograms during the co-flow injection of $CaCl_2$ in a solution of 50% $D_2O$ + 50% $H_2O$ (blue color) and $Na_2CO_3$ in a solution of 100% $D_2O$ (red color) for the experiment Basalt-PSI. A zoom-in figure is included to highlight the preferential flow channel at $t = 98$ min occupied by the 100% $D_2O$ solution.

sample, for the fluids 50% $D_2O$ + 50% $H_2O$ (Figure 10a) and 100% $D_2O$ (Figure 10b), and the precipitates (Figure 10c). The *Y*-direction in the middle of the slice corresponds to the physical barrier of the core holder at the top of the rock that initially separated the two injected fluids, causing a co-flow of the two miscible fluids through the sample. As shown in Figure 10c, there is a higher density of calcite precipitation at the interface, which is consistent with classical transverse mixing and reaction processes (Cirpka et al., 2015; Tartakovsky et al., 2008). The density profile perpendicular to the interface in Figure 10d further illustrates the pronounced concentration of calcite precipitates along the fluid interface. The results also indicate that while transverse mixing drives primary calcite precipitation at the interface during the injection process, diffusive mixing after the experiments contributes to further calcite formation in areas away from the interface.

To further explore the relationship between fluid mixing and precipitation, we attempted to correlate fluid concentrations obtained from the final neutron tomogram with the distribution of precipitates from the high-resolution X-ray 3 scan of Basalt-ILL. After resampling and registering both volumes, we averaged both the segmented precipitation and the extracted fluid concentration over coarsened 8-voxel blocks. The resulting scatter and density plots in the Figure S3 of Supporting Information S1 show the fraction of precipitation versus average fluid concentration in each block. While we expected a peak in precipitation fraction at intermediate concentrations, where both fluids are present, no clear trend was observed. This indicates significant post-experiment diffusive-mixing and redistribution of fluids had occurred throughout the rock, leading to precipitation beyond the original mixing zone. These effects hinder possible spatial correlation between the initial mixing zone and the location of precipitates observed 6 months later.

### 4.2. Experiment Basalt-PSI

#### 4.2.1. 4D Neutron Imaging of Fluid Mixing

The Basalt-PSI experiment was performed with a scan duration of 49 min and a flow rate ($Pe = 1.7$) lower than for the other experiment. Figure 11 displays a rendering and orthogonal views of the series of neutron tomograms acquired during the experiment ($Pe = 1.7$), illustrating the gradual mixing of the injected fluids into the basalt sample. Initially, despite the injection of $D_2O$ before the co-flow, the rock remained unintentionally unsaturated, as shown in the image at $t = 98$ min, which displays many empty pores. This was likely due to the low permeability and heterogeneous pore structure of the sample, which hindered complete air displacement. Consequently, unlike the experiment Basalt-ILL, the mixing process involved a large extent of multiphase transport, with the pores gradually filled by the injected fluids that replaced the air. We initially observed that a primary, preferential channel was filled by the solution 100% $D_2O$. As the co-flow injection continued, the mixing of the fluids became apparent. After $t = 294$ min, we observe different fluid flow pathways and preferential channels of the two fluids, suggesting that calcium carbonate precipitation has altered the flow pathways.

Similar to the Basalt-ILL experiment, we used the initial X-ray image for the Basalt-PSI experiment to segment the solid-phase distribution and then extracted the pore volumes filled with air or the injected fluids from the neutron tomograms. Subsequently, we segmented the two fluids (100% $D_2O$ and 50% $D_2O$ + 50% $H_2O$) and the empty pores from the time-lapse neutron images. The linear attenuation coefficients of the extracted fluids were scaled between 0 and 1, corresponding to their relative concentration. Figure 12a displays the probability density

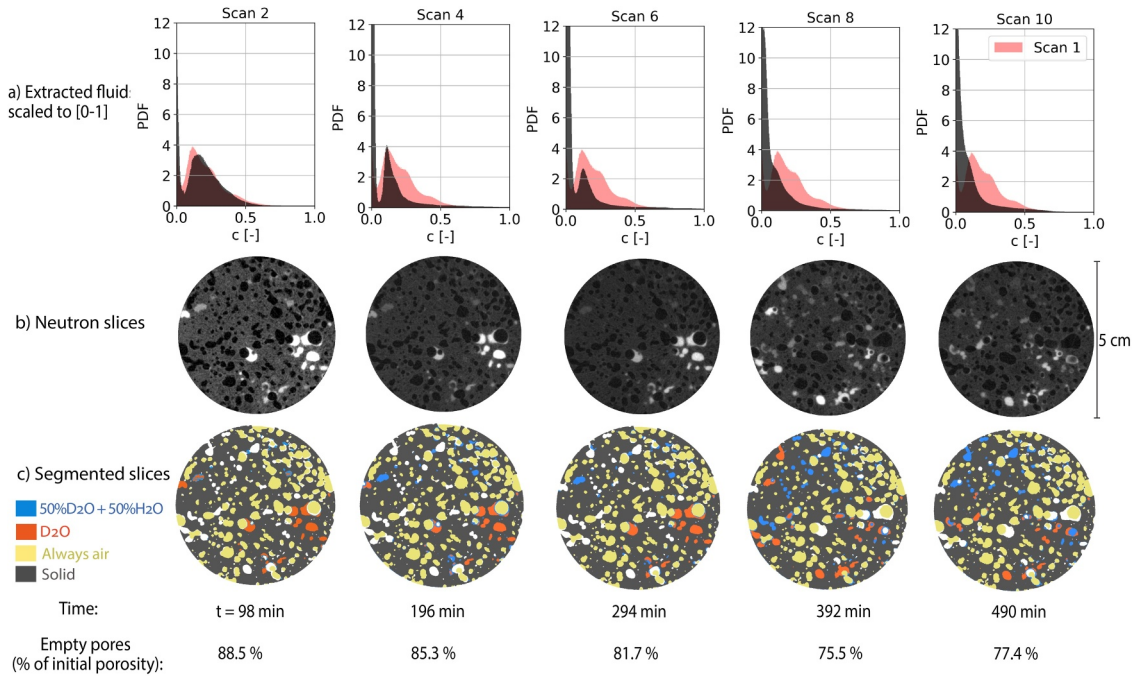


**Figure 12.** (a) Probability density function of the concentration of the fluids extracted from neutron tomograms for the Basalt-PSI experiment. The initial reference distribution from scan 1 ($t$ = 49 min) is overlaid in red on each histogram. (b) Horizontal slices of neutron scans at the center of the sample rock at different times. (c) Segmentation of the corresponding slices into the two fluids, the empty pores that are consistently filled with air, and the solid phase. The percentage of empty pores relative to the initial porosity at each time step is also reported.

function of the normalized concentration in the whole sample. As a reference, the distribution from the initial scan ($t$ = 49 min) is overlaid in red on each panel to illustrate how the concentration changes over time. Initially, a higher range of concentration values is marked by a peak in the distribution, indicating the presence of primarily $D_2O$. As the co-flow injection progressed, the peak shifts and merges to the left, indicating that the 50% $D_2O$ + 50% $H_2O$ fluid increasingly replaced the pore spaces and mixed with $D_2O$. Figures 12b and 12c show two-dimensional slices of the neutron scans and the corresponding segmented slices, taken from the middle of the basalt sample. The segmentation of these slices into the two fluids, the empty pores consistently filled with air, and into the solid phase is further illustrated for other heights of the sample rock in the Figures S4 and S5 of Supporting Information S1. The pores shown in yellow are filled with air, indicating either a lack of connectivity or exclusion from the fluid pathways. From the slices, it appears that at the initial stage of the injection, a larger proportion of the fluid present was $D_2O$. As the injection continued, the fluid with 50% $D_2O$ + 50% $H_2O$ progressively filled the pore space. The dynamic fluid displacement indicates the presence of multiphase flow in the sample.

The volume fraction of the two fluids and of the empty pores through the height of the rock at different times are presented in Figures 13a–13c. By comparing the curves for the fraction of 100% $D_2O$ filled pores throughout the height at different times (Figure 13a), it appears that the proportion of this solution remains relatively constant throughout the co-flow injection. The proportion of the fluid with 50% $D_2O$ + 50% $H_2O$ throughout the height, as shown in Figure 13b, increases over time, indicating that this solution progressively occupied more pores in the rock. This trend is further confirmed by Figure 13c, which shows that the fraction of pores containing air is decreasing over time, reflecting the fact that fluids were filling the previously air-filled pores. Figure 13d shows how the composition of the fluid-filled pores changes over time, with a gradual increase in the proportion of 50% $D_2O$ + 50% $H_2O$. Figure 13e shows the percentage of empty pores relative to the initial porosity of 35.9%, indicating a gradual decrease in empty pores and an increase in fluid saturation as the injection progressed.

To estimate the extent of mixing between the injected fluids, we analyze the scaled attenuation coefficients of the extracted fluids, as indicated by the concentration values in Figure 12a. Figure 14a presents the mean concentration, along with the variance of concentration $\sigma^2$ as a metric for mixing in the whole sample. The mean

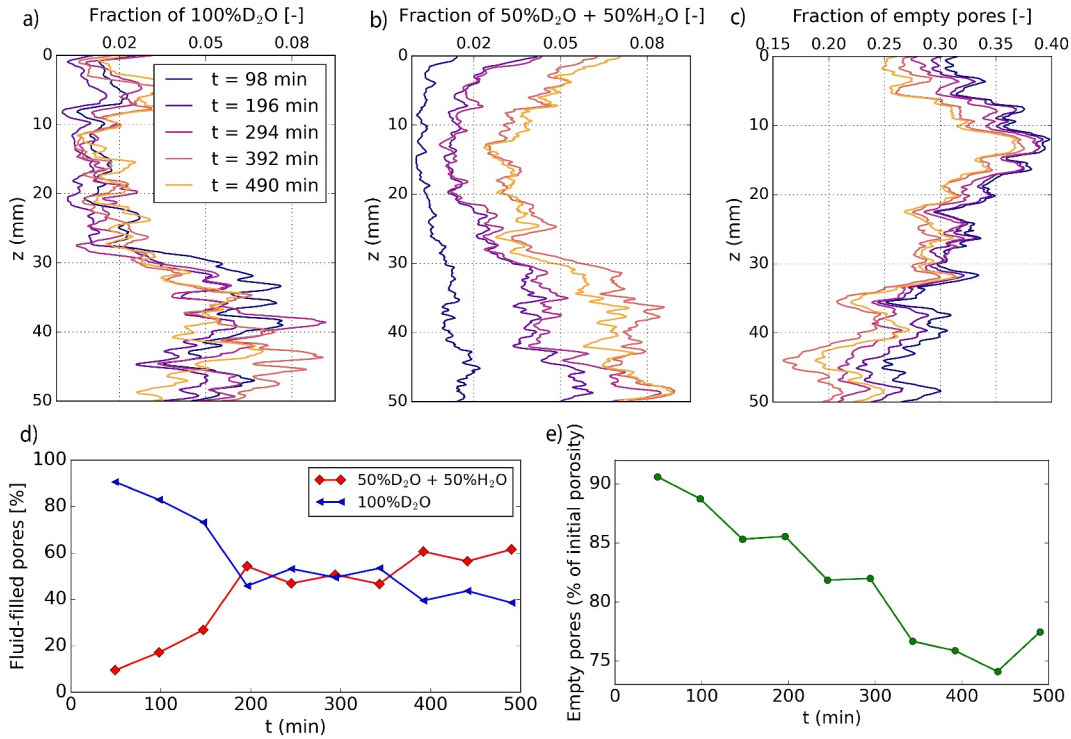


**Figure 13.** Segmentation analysis of neutron tomograms from experiment Basalt-PSI, illustrating the volume fraction of fluid 100% $D_2O$ (a), fluid 50% $D_2O$ + 50% $H_2O$ (b), and empty pores (c) as a function of height at different time points. Panel (d) shows the percentage of the fluid-filled pore volume occupied by each injected fluid over time. Panel (e) shows the evolution of the empty pore volume, expressed as a percentage of the initial porosity (35.9%).

concentration curve shows a decrease after three scans ($t = 147$ min), indicating that the pores are increasingly occupied by 50% $D_2O$ + 50% $H_2O$. Meanwhile, the curve showing $\sigma^2$ exhibits an increase after that time, reflecting a greater presence of the second fluid within the rock and an increase in the spread of concentration values around the mean. The oscillations in the mean concentration after $t = 196$ min correspond to the interactive movement of the two fluids and the replacement of air by the fluids during the multiphase flow and mixing processes. The value of $\sigma^2$ shows a decline after $t = 294$ min, indicating more effective mixing and consequently lower variability in concentration. The variance of concentration along the core sample, at different times (Figure 14b) shows significant fluctuations, indicating heterogeneity in the mixing process. The mean concentration profile in Figure 14c also exhibits noticeable variability along the height of the sample indicating that fluid distribution and replacement were not uniform. Furthermore, similar to the analysis in Section 4.1.3, the mean segmentation density plots of fluids for the Basalt-PSI experiment, as presented in Figure S7 of Supporting Information S1, does not show a clear transverse mixing pattern, contrary to the Basalt-ILL experiment. This is consistent with the strong spatial heterogeneity of mixing patterns.

### 4.2.2. X-Ray Imaging of Filled Pores at PSI

X-ray tomography scans during the Basalt-PSI experiment were acquired before and after mineral precipitation. Similar to the previous experiment, fluid injection was paused during the X-ray 1 and X-ray 2 scans, likely allowing some fluid movement due to gravity and atmospheric pressure in the outlet tubes. Figure 15a presents two-dimensional slices of the basalt core perpendicular to the core axis at different heights, captured before (X-ray 1) and after (X-ray 2) the co-injection of $Na_2CO_3$ (100% $D_2O$) and $CaCl_2$ (50% $D_2O$ + 50% $H_2O$) solutions. The increased number of filled pores due to the presence of more fluids and calcite precipitation can be deduced by comparing scan X-ray 2 to scan X-ray 1, although X-ray tomography data does not allow us to differentiate clearly between the fluid phase and the unconsolidated calcite crystals.

Figure 15b displays the difference between the corresponding slices at different heights, highlighting the changes in the pore filling between the beginning and the end of the experiment. Since the rock became more saturated and

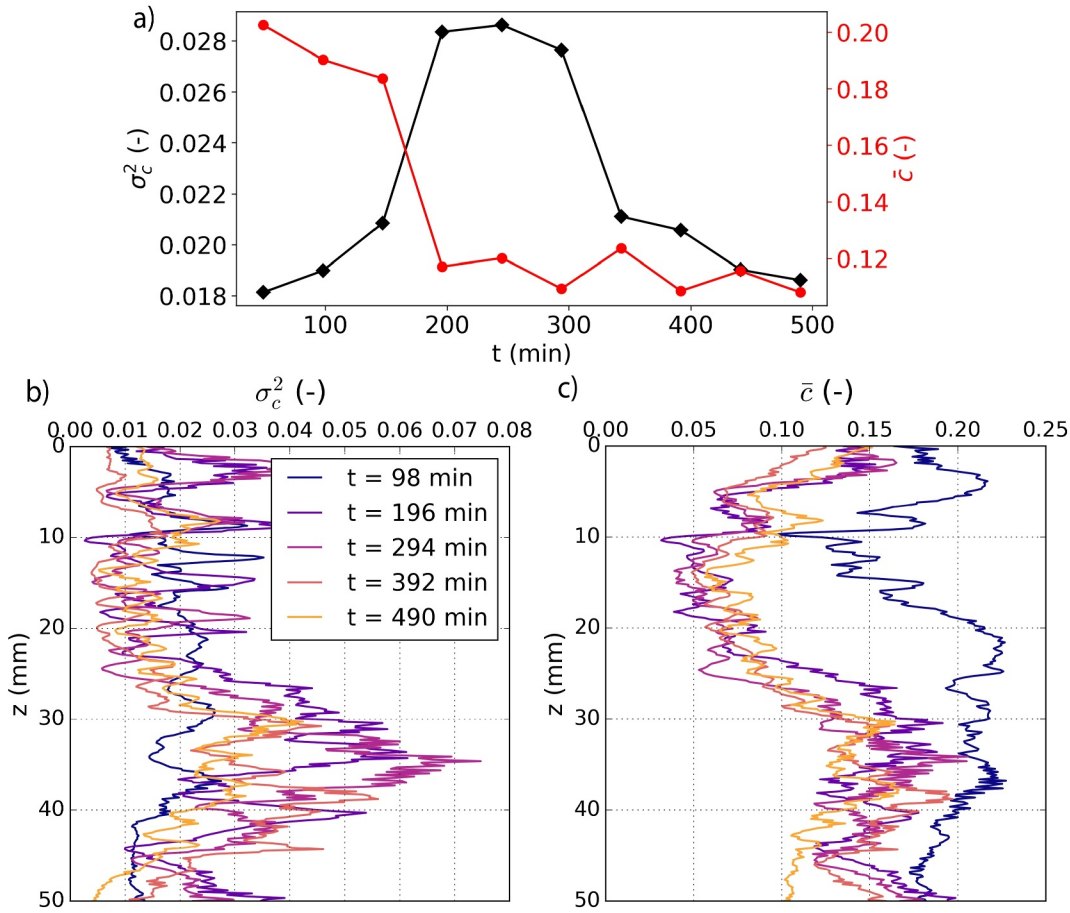


**Figure 14.** (a) Mean concentration of the extracted fluids (red curve with the ordinate on the right) and variance of the concentration (black curve with the ordinate on the left) through time for the experiment Basalt-PSI. The variation of (b) variance and (c) mean concentration through height is shown at different times.

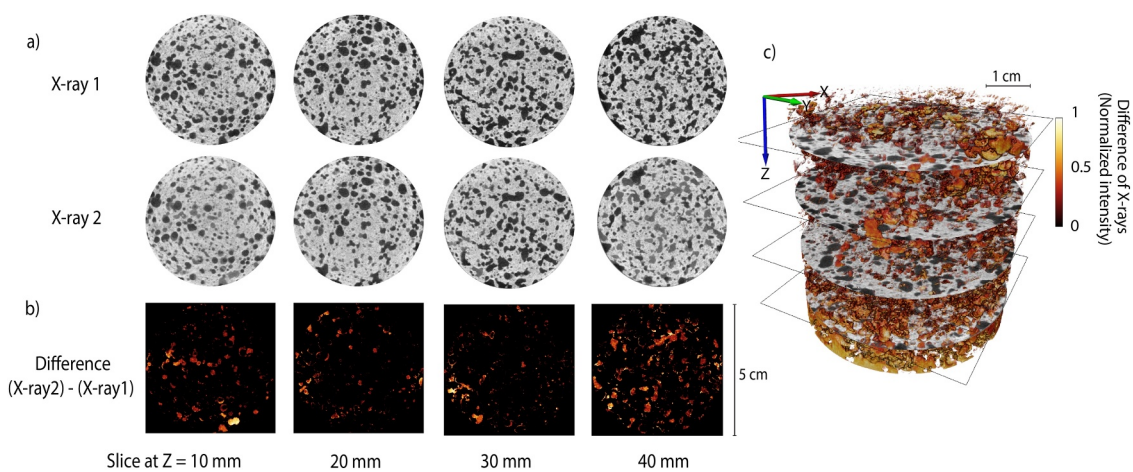


**Figure 15.** X-ray images of experiment Basalt-PSI: (a) tomography slices perpendicular to the core axis at different heights before (X-ray 1) and after (X-ray 2) precipitation acquired at PSI with a voxel size of 42.95 µm. (b) The difference of the corresponding slices at different heights. (c) Volume rendering of the difference of the X-ray images showing the heterogeneous distribution of fluids and precipitates.

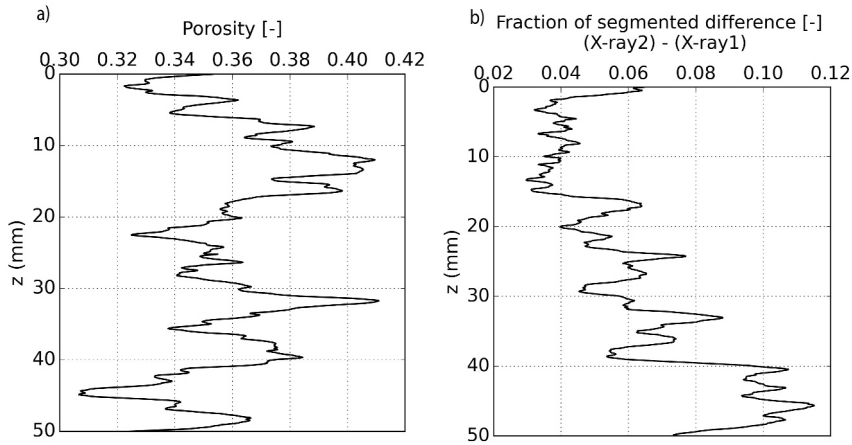


**Figure 16.** (a) Porosity distribution profile along the core sample axis for the Basalt-PSI experiment, calculated by dividing the total segmented pore volume by the slice surface area in X-ray 1. (b) Profile illustrating the fraction of segmented differences between scans X-ray 2 and X-ray 1 (segmented difference divided by slice surface area), indicating the proportion of pores filled with injected fluids and calcite precipitates.

the difference is positive, the normalized difference primarily indicates that the pores are being filled with fluids or precipitates during the experiment. The density of calcite in the images is slightly higher than that of the fluids, resulting in a range of intensity in the image of the difference. Regions with brighter yellow color represent domains with higher density in the difference, which corresponds to saturated pores that contain more calcite crystals. In contrast, as the color shifts toward darker shades, it indicates lower density in the difference, which corresponds to regions with progressively lower X-ray adsorption, and less to no calcite. Figure 15c shows a three-dimensional rendering of the difference between the X-ray 1 and X-ray 2 scans, showing a visual representation of the extent of pores filled with fluids and mineral precipitates.

Figure 16a shows the porosity distribution profile along the core sample, calculated by dividing the total segmented pore volume by the total surface area in image X-ray 1. Since the precipitates are not fully consolidated into solid phases, the segmented pore volumes derived from X-ray 1 and X-ray 2 do not show a significant difference. There are significant initial porosity variations throughout the height of the sample, indicating the presence of large pores, which also appear in the two-dimensional slices shown in Figure 15a. This variation in porosity reflects the heterogeneous nature of the basalt core, with certain regions containing significantly more pore space than others. Figure 16b illustrates the fraction of segmented differences between X-ray 2 and X-ray 1, indicating the proportion of pores filled with injected fluids and calcite precipitates. The profile shows that the bottom of the rock has a higher fraction of filled pores, which is in agreement with the findings of the fluid fraction analysis (Figures 13a and 13b).

## 5. Discussion

### 5.1. Pore Scale Imaging and Its Implications

The coupling of neutron and X-ray tomography was designed to provide pore scale images of fluid mixing and mineral precipitation in rocks. Neutron imaging, with its sensitivity to hydrogen atoms and its isotopic forms, allowed distinguishing between the two injected miscible fluids ($D_2O$ and 50% $D_2O$ + 50% $H_2O$) and quantifying their interaction and mixing over time. X-ray imaging, on the other hand, complemented the neutron data by offering high-resolution structural information about the solid matrix, and the filling of the pores with crystal precipitates and fluid presence or absence (without the capacity to distinguish the two isotopes). Imaging the dynamic evolution of fluid distribution and the spatial localization of solid-phase changes requires synchronized, high-resolution, and real-time imaging with both methods.

With the current technology, time-lapse neutron imaging of a sample rock with the size of a few centimeters allows for temporal resolutions ranging from 5 min to 1 hr, depending on the spatial resolution required (and flux available), which typically falls within the range of tens of μm (Tengattini et al., 2021). Achieving a reasonable scanning time of less than an hour can limit the ability to resolve pore structures in centimeter-sized rocks with

**Table 1**
*Porosity and Air/Fluid Saturations for Basalt-ILL and Basalt-PSI Experiments*

| Porosity (%) | Basalt-ILL | Basalt-PSI |
|---|---|---|
| Initial | 36.8 | 35.9 |
| Always filled with air | 22.1 | 25.4 |
| Always filled with fluids | 11.2 | 1.3 |
| Alternating fluid and air | 3.5 | 9.2 |

pore diameters of 200 μm or smaller, such as sandstone (Shafabakhsh, Cordonnier, et al., 2024). In contrast, X-ray imaging excels in high-resolution petrophysical studies, where resolutions range from nanometers to a few μm (Arif et al., 2021). While combining neutron and X-ray imaging is attractive, simultaneous acquisition of X-ray and neutron imaging is challenging due to the disparity in spatial and temporal resolutions between the two techniques, where optimizing one can come at the expense of the other (Chiang et al., 2018; Tengattini et al., 2021). In addition, the physical setup required for simultaneous imaging is more complex, particularly in aligning the instruments to achieve accurate and synchronized data collection. Despite the challenges, this integration is feasible under specific conditions, depending on the sample size and required resolutions, at a few facilities worldwide, including ILL (Tengattini et al., 2020) and PSI (A. Kaestner et al., 2015). Ongoing advancements in imaging technology and synchronization methods will further improve the integration of these techniques for desirable spatial and temporal resolutions, enabling more detailed real-time studies of complex geological processes.

In this work, the application of time-lapse neutron and X-ray imaging to investigate dynamic fluid mixing and visualize pore-scale processes revealed several methodological challenges that impact data interpretations. First, the spatial resolution of the X-ray scans acquired before and after the experiment (scans X-ray 1 and X-ray 2) was not sufficient to resolve early stage and unconsolidated crystal precipitates, particularly since these mineral phases often shared attenuation values with the surrounding fluids, making them indistinguishable for segmentation. Moreover, the temporal separation between neutron and X-ray acquisitions limited our ability to establish a direct correlation between fluid mixing and precipitation, as the system evolved in the time between imaging sessions. Segmenting the neutron images was further complicated because of overlapped voxel intensities among different fluid phases, partial volume effects, and imaging noise. Beyond imaging-specific limitations, experimental constraints also played a role. Achieving full saturation in the basalt cores was difficult due to isolated and poorly connected pores, and this issue was amplified by the need for a low flow rate, particularly in the Basalt-PSI experiment, where long neutron scan times required slower flows to avoid image blurring effect. At such low rates, gravitational drainage became more pronounced, promoting fluid loss and persistent air entrapment that led to multiphase flow conditions throughout the injection period. Together, these technical and experimental challenges highlight areas where further methodological improvements are needed.

### 5.2. Fluid Mixing in Steady Versus Unsteady Flows

Although the occurrence of multiphase flow of air and water in the second experiments was initially unwanted, the comparison with the first experiment where multiphase flow was limited allows testing the method for both steady and unsteady mixing fronts. In steady flows, reactive fluids flowing in parallel mix and react under the combined action of heterogeneous advection at the pore scale and diffusion. The presence of a moving second phase can enhance solute mixing, dispersion and reaction in the first fluid phase by generating transient flow dynamics, as shown for idealized 2D porous media (Mathiesen et al., 2023; X. Zhang et al., 2025).

Table 1 shows the porosity and fluid/air saturation characteristics for the Basalt-ILL and Basalt-PSI experiments obtained from the segmentation of neutron tomograms, which provides insights into the extent of multiphase flow in the experiments. Notably, the percentage of porosity exhibiting an alternation of fluid and air phases (which directly contributes to multiphase flow dynamics) was 3.5% in the Basalt-ILL experiment and 9.2% in the Basalt-PSI experiment. For both experiments, almost two-thirds of the porosity was consistently filled with air, indicating pores that were either not connected or not part of the flow pathways.

The Basalt-ILL experiment exhibited a steady transverse mixing, with a small amount of multiphase flow. The analysis of concentration variance showed a relatively stable mixing process, with low fluctuations in concentration variance over time (Figure 7a) and a decay of the variance as a function of the depth inside the sample (Figure 7b). In the Basalt-PSI experiment, the mixing process was characterized by a higher degree of heterogeneity in extracted fluid distribution, likely resulting in more dispersed regions of calcite precipitation. The occurrence of multiphase flow with moving air during the injection also allowed for more interaction between the solutions $CaCl_2$ and $Na_2CO_3$, thereby enhancing mixing. The dynamic fluid displacement observed through segmentation caused the mixing process to become more effective over time by enhancing the contact area

between the two fluids in the pore space, as indicated by the decrease of the global concentration variance $\sigma^2$ after prolonged injection ($t = 294$ min) in Figure 14.

The observed differences in fluid mixing between the two experiments may be attributed to multiple factors, including flow rate, pore structure, saturation state, and air entrapment. The two sample cores, although extracted from the same basalt block, displayed visible differences in internal heterogeneity, as seen in their pore size distributions. These structural differences likely influenced how fluids propagated, interacted, and displaced one another. Furthermore, the lower flow rate used in the Basalt-PSI experiment not only altered the advection–diffusion balance but also amplified the effect of gravity, promoting fluid drainage and making it more difficult to maintain saturation during the co-flow injection. This led to persistent multiphase conditions, with air remaining in the system and affecting the mixing process. These contributing factors in the differences between the two experiments (pore structure, flow rate, and air entrapment) were closely interrelated in their effects, making it difficult to quantify their individual influence on the overall outcome.

Although the fraction of segmented difference between scans X-ray 2 and X-ray 1 for the Basalt-ILL experiment (Figure 9b) appears lower than that of Basalt-PSI (Figure 16b), this does not conclusively indicate a difference in calcite production, since the fluids filling the empty pores during both experiments are also included in the difference and the X-ray sources in these two experiments were different. The segmented precipitation from the high-resolution tomogram X-ray 3 acquired at ESRF and shown in Figure 9c highlights the amount of calcite produced during the 6-month period of diffusive mixing, along with other potential salt precipitates that may have formed after evaporation within the pores, as discussed in Section 5.3.

### 5.3. Calcite Precipitation During and After Fluid Mixing

While the methodology has potential to link mixing to precipitation in rocks, the presented experiments revealed some limitations, such as spatial and temporal resolution mismatches, segmentation uncertainties, and challenges in saturation control that prevented us from conclusively reaching this objective. In both experiments, a greater amount of filled pores was observed near the bottom of the cores, as calculated from the segmentation of the difference between tomograms X-ray 2 and X-ray 1 (Figures 9b and 16b). This observation may indicate an enhanced mixing and subsequent chemical reactions in lower regions. However, a contributing factor could be the fact that fluid injection was paused during the X-ray 1 and X-ray 2 scans, and due to gravity and pressure gradients at the outlet tubes, some fluids may have migrated downward. The comparison of scans X-ray 1 and X-ray 2 could not allow distinguishing the unconsolidated precipitates from the fluids because they had similar attenuation values, and the early stage crystal precipitates were below the resolution threshold.

The high-resolution X-ray 3 scan of the dried Basalt-ILL sample acquired after 6 months provided a detailed view of the precipitations formed within the pores. A significant amount of calcite precipitation was likely driven by transverse mixing during the injection process at the interface between the two reactive fluids as discussed in Section 4.1.3. Some additional calcite precipitation occurred over time, driven by diffusive mixing. To estimate the timescale of this diffusive mixing, we assume that half of the core (with the radius of $R = 2.5$ cm) was saturated with solution $CaCl_2$ and the other half with solution $Na_2CO_3$. Given a diffusion coefficient of $D = 9.4 \times 10^{-10}\,m^2\,s^{-1}$, the characteristic diffusion time is $\tau_d = R^2/D \simeq 1$ week. This result suggests that significant diffusion-driven mixing and additional calcite precipitation continued in the week following the experiment Basalt-ILL. Note that due to the high solubility of the salts $CaCl_2$, $Na_2CO_3$, and the produced NaCl salt after the reaction, it is unlikely that these precipitates formed during the injection process. However, during the 6-month drying period, the evaporation of the remaining solutions in the basalt rock could have led to the precipitation of NaCl, in addition to the calcite. Distinguishing between these different types of precipitates, however, is not feasible using our X-ray imaging data.

To estimate an upper bound the amount of mineral precipitation in the Basalt-ILL sample, we consider that a total of 2.2 pore volumes of reactive fluids were injected during the experiment. Given the 1 M concentration of $CaCl_2$ and $Na_2CO_3$ solutions, and assuming complete mixing and reaction, this would lead to the precipitation of approximately 1.4 $cm^3$ of $CaCO_3$, based on reaction stoichiometry, a molar mass of calcite of 100.09 g/mol, and a density of 2.71 $g/cm^3$. Additionally, NaCl is also produced from the reaction between the two injected solutions. However, due to its high solubility of 6 M, we assume that NaCl did not precipitate during the injection phase. Instead, NaCl precipitation occurred only after the experiment, driven by evaporation during the 6-month drying

period. Since the injected fluids occupied approximately one-third of the pore volume, and assuming full evaporation of this fraction, we estimate the resulting NaCl precipitation to be around 0.3 $cm^3$. The segmented volume of precipitates from the high-resolution X-ray scan (Figure 9c) corresponds to 0.034 of the total sample volume, which is equivalent to approximately 3.4 $cm^3$. This is noticeably higher than the upper bound estimate of $CaCO_3$ and NaCl precipitation (1.4 + 0.3 $cm^3$). Several factors may contribute to this discrepancy. First, it is plausible that reactive fluids may have remained within the porous glass spacers at the top of the core, allowing for continued transport and precipitation beyond the core volume considered in the estimate. Second, microporosity within the precipitated minerals may result in an overestimation of the solid volume when segmented based on attenuation contrast. Finally, segmentation thresholds may also capture mixed voxels or residual salts that increase the apparent precipitate volume.

## 6. Conclusion

The presented experiments provide new insights on the potential and challenges of using combined neutron and X-ray imaging to monitor fluid mixing and precipitation in rocks at the pore-to-core scale. Time-lapse neutron imaging provided a detailed temporal evolution of the distribution of the injected miscible fluids, distinguishing them thanks to the different isotopic ratios, with minimal density-driven flow. X-ray imaging, on the other hand, complemented the neutron data by offering high-resolution structural information, particularly in visualizing the solid phase, and using it as a mask to extract the fluid phase in the neutron data.

The Basalt-ILL experiment showed a steady transverse mixing pattern, with a narrow mixing zone at the interface of the two injected fluids. In contrast, in the Basalt-PSI experiment the motion of trapped air clusters, which could not be removed during the initial saturation, promoted temporal fluctuations in the distribution of fluids, leading to enhanced mixing. The intermittent motion of air clusters may have been due to the lower flow rate but also to structural differences between the core samples. Although both samples in this study were sourced from the same bulk basalt, internal heterogeneity, both between and within cores, likely contributed to the observed differences in flow and mixing dynamics between the two experiments. High-resolution X-ray imaging of the sample Basalt-ILL revealed that calcite formation continued to occur as a result of long-term diffusive mixing, indicating ongoing reactions after the experiment.

Several methodological limitations affected data interpretation. The spatial resolution of the X-ray scans was insufficient to detect early stage or unconsolidated precipitates, which often had similar attenuation values to surrounding fluids. Temporal gaps between neutron and X-ray acquisitions hindered direct correlation between fluid mixing and mineral precipitation. Additionally, segmentation of neutron images was challenged by overlapping voxel intensities, partial volume effects, and imaging noise.

While at this stage, the technique did not allow deriving quantitative constitutive relationships between fluid mixing and precipitation, results highlight the capabilities and current limitations of this dual-imaging approach. By capturing both fluid dynamics and precipitation patterns in the same core samples, this framework provides a basis for future studies to quantify local mixing, reactive surface evolution, and mineralization rates. Future experiments may focus on advancing joint 4D imaging using X-ray and neutron tomography. Simultaneous imaging should likely provide more detailed insights into how fluid interactions drive mineralization processes. Furthermore, extending this work to include long-term experiments, spanning several weeks or months, would provide valuable data on the time evolution of reactive transport and mineralization processes. The experiments should be designed with precise control of the boundary conditions to enable comparisons with numerical simulations of calcite precipitation, enhancing model validation and predictive accuracy. The application of this experimental and modeling framework to $CO_2$ mineral trapping in basalt reservoirs will be important in advancing carbon sequestration technologies.

## Conflict of Interest

The authors declare no conflicts of interest relevant to this study.

## Data Availability Statement

The 3D reconstructed neutron and X-ray scans from PSI, ILL, and ESRF, along with the raw data are available at Shafabakhsh (2024) [Dataset]: https://doi.org/10.11582/2024.00144.

**Acknowledgments**
The study received funding from the Akademiaavtalen (Academic Agreement) between Equinor and the University of Oslo through the project MODIFLOW. GL acknowledges support from the Research Council of Norway through Grants 325819 (M4) and 262644 (PoreLab Center of Excellence). F.R. acknowledges support from the project FricFrac funded by the Center for Advanced Study at the Norwegian Academy of Science and Letters during the academic year 2023–2024, and from Sigma2 (project NS9073K). The basalt samples have been obtained through the SUCCEED program (funded by Accelerating CCS Technologies, Project No 294766), with special thanks to Orkuveita Reykjavíkur/ Reykjavik Energy Iceland.

## References

Anna, P. D., Jimenez-Martinez, J., Tabuteau, H., Turuban, R., Le Borgne, T., Derrien, M., & Méheust, Y. (2014). Mixing and reaction kinetics in porous media: An experimental pore scale quantification. *Environmental Science & Technology*, *48*(1), 508–516. https://doi.org/10.1021/es403105b

Aradóttir, E., Sonnenthal, E., Björnsson, G., & Jónsson, H. (2012). Multidimensional reactive transport modeling of $CO_2$ mineral sequestration in basalts at the Hellisheidi geothermal field, Iceland. *International Journal of Greenhouse Gas Control*, *9*, 24–40. https://doi.org/10.1016/j.ijggc.2012.02.006

Arif, M., Mahmoud, M., Zhang, Y., & Iglauer, S. (2021). X-ray tomography imaging of shale microstructures: A review in the context of multiscale correlative imaging. *International Journal of Coal Geology*, *233*, 103641. https://doi.org/10.1016/j.coal.2020.103641

Bandopadhyay, A., Davy, P., & Le Borgne, T. (2018). Shear flows accelerate mixing dynamics in hyporheic zones and hillslopes. *Geophysical Research Letters*, *45*(21), 11–659. https://doi.org/10.1029/2018gl079914

Bauer, R. D., Maloszewski, P., Zhang, Y., Meckenstock, R. U., & Griebler, C. (2008). Mixing-controlled biodegradation in a toluene plume—results from two-dimensional laboratory experiments. *Journal of Contaminant Hydrology*, *96*(1–4), 150–168. https://doi.org/10.1016/j.jconhyd.2007.10.008

Bhandari, N., Kan, A. T., Zhang, F., Dai, Z., Yan, F., Ruan, G., et al. (2016). Mineral precipitation kinetics: Assessing the effect of hydrostatic pressure and its implication on the nucleation mechanism. *Crystal Growth & Design*, *16*(9), 4846–4854. https://doi.org/10.1021/acs.cgd.6b00126

Bochet, O., Bethencourt, L., Dufresne, A., Farasin, J., Pédrot, M., Labasque, T., et al. (2020). Iron-oxidizer hotspots formed by intermittent oxic–anoxic fluid mixing in fractured rocks. *Nature Geoscience*, *13*(2), 149–155. https://doi.org/10.1038/s41561-019-0509-1

Boon, M., Bijeljic, B., & Krevor, S. (2017). Observations of the impact of rock heterogeneity on solute spreading and mixing. *Water Resources Research*, *53*(6), 4624–4642. https://doi.org/10.1002/2016wr019912

Boon, M., Bijeljic, B., Niu, B., & Krevor, S. (2016). Observations of 3-D transverse dispersion and dilution in natural consolidated rock by X-ray tomography. *Advances in Water Resources*, *96*, 266–281. https://doi.org/10.1016/j.advwatres.2016.07.020

Bultreys, T., De Boever, W., & Cnudde, V. (2016). Imaging and image-based fluid transport modeling at the pore scale in geological materials: A practical introduction to the current state-of-the-art. *Earth-Science Reviews*, *155*, 93–128. https://doi.org/10.1016/j.earscirev.2016.02.001

Chang, R., Kim, S., Lee, S., Choi, S., Kim, M., & Park, Y. (2017). Calcium carbonate precipitation for $CO_2$ storage and utilization: A review of the carbonate crystallization and polymorphism. *Frontiers in Energy Research*, *5*, 17. https://doi.org/10.3389/fenrg.2017.00017

Chen, Y., Steeb, H., Erfani, H., Karadimitriou, N. K., Walczak, M. S., Ruf, M., et al. (2021). Nonuniqueness of hydrodynamic dispersion revealed using fast 4D synchrotron X-ray imaging. *Science Advances*, *7*(52), eabj0960. https://doi.org/10.1126/sciadv.abj0960

Chiang, W.-S., LaManna, J. M., Hussey, D. S., Jacobson, D. L., Liu, Y., Zhang, J., et al. (2018). Simultaneous neutron and X-ray imaging of 3D structure of organic matter and fracture in shales. *Petrophysics*, *59*(2), 153–161. https://doi.org/10.30632/pjv59n2-2018a3

Cirpka, O. A., Chiogna, G., Rolle, M., & Bellin, A. (2015). Transverse mixing in three-dimensional nonstationary anisotropic heterogeneous porous media. *Water Resources Research*, *51*(1), 241–260. https://doi.org/10.1002/2014wr015331

Cirpka, O. A., Olsson, Å., Ju, Q., Rahman, M. A., & Grathwohl, P. (2006). Determination of transverse dispersion coefficients from reactive plume lengths. *Groundwater Series*, *44*(2), 212–221. https://doi.org/10.1111/j.1745-6584.2005.00124.x

Cnudde, V., & Boone, M. N. (2013). High-resolution X-ray computed tomography in geosciences: A review of the current technology and applications. *Earth-Science Reviews*, *123*, 1–17. https://doi.org/10.1016/j.earscirev.2013.04.003

Cole, D. R., Herwig, K. W., Mamontov, E., & Larese, J. Z. (2006). Neutron scattering and diffraction studies of fluids and fluid-solid interactions. *Reviews in Mineralogy and Geochemistry*, *63*(1), 313–362. https://doi.org/10.2138/rmg.2006.63.13

Coles, M., Hazlett, R., Muegge, E., Jones, K., Andrews, B., Dowd, B., et al. (1998). Developments in synchrotron X-ray microtomography with applications to flow in porous media. *SPE Reservoir Evaluation and Engineering*, *1*(4), 288–296. https://doi.org/10.2118/50985-pa

Cordonnier, B., Pluymakers, A., Tengattini, A., Marti, S., Kaestner, A., Fusseis, F., & Renard, F. (2019). Neutron imaging of cadmium sorption and transport in porous rocks. *Frontiers in Earth Science*, *7*, 306. https://doi.org/10.3389/feart.2019.00306

Dai, Z., Xu, L., Xiao, T., McPherson, B., Zhang, X., Zheng, L., et al. (2020). Reactive chemical transport simulations of geologic carbon sequestration: Methods and applications. *Earth-Science Reviews*, *208*, 103265. https://doi.org/10.1016/j.earscirev.2020.103265

Danckwerts, P. (1952). The definition and measurement of some characteristics of mixtures. *Applied Scientific Research, Section A*, *3*(4), 279–296. https://doi.org/10.1007/bf03184936

Dávila, G., Dalton, L., Crandall, D. M., Garing, C., Werth, C. J., & Druhan, J. L. (2020). Reactive alteration of a Mt. Simon sandstone due to $CO_2$-rich brine displacement. *Geochimica et Cosmochimica Acta*, *271*, 227–247. https://doi.org/10.1016/j.gca.2019.12.015

Deng, H., Tournassat, C., Molins, S., Claret, F., & Steefel, C. (2021). A pore-scale investigation of mineral precipitation driven diffusivity change at the column-scale. *Water Resources Research*, *57*(5), e2020WR028483. https://doi.org/10.1029/2020wr028483

Dentz, M., Hidalgo, J. J., & Lester, D. (2023). Mixing in porous media: Concepts and approaches across scales. *Transport in Porous Media*, *146*(1), 5–53. https://doi.org/10.1007/s11242-022-01852-x

De Vriendt, K., Le Borgne, T., Pool, M., & Dentz, M. (2022). Subsurface mixing dynamics across the salt-freshwater interface. *Geophysical Research Letters*, *49*(7), e2021GL097094. https://doi.org/10.1029/2021gl097094

Disch, J., Bohn, L., Koch, S., Schulz, M., Han, Y., Tengattini, A., et al. (2022). High-resolution neutron imaging of salt precipitation and water transport in zero-gap $CO_2$ electrolysis. *Nature Communications*, *13*(1), 6099. https://doi.org/10.1038/s41467-022-33694-y

Emmanuel, S., & Berkowitz, B. (2005). Mixing-induced precipitation and porosity evolution in porous media. *Advances in Water Resources*, *28*(4), 337–344. https://doi.org/10.1016/j.advwatres.2004.11.010

Gysi, A. P., & Stefánsson, A. (2012). $CO_2$-water–basalt interaction. Low temperature experiments and implications for $CO_2$ sequestration into basalts. *Geochimica et Cosmochimica Acta*, *81*, 129–152. https://doi.org/10.1016/j.gca.2011.12.012

Haide, R., Fest-Santini, S., & Santini, M. (2022). Use of X-ray micro-computed tomography for the investigation of drying processes in porous media: A review. *Drying Technology*, *40*(9), 1731–1744. https://doi.org/10.1080/07373937.2021.1876723

Harrison, A. L., Dipple, G. M., Power, I. M., & Mayer, K. U. (2016). The impact of evolving mineral–water–gas interfacial areas on mineral–fluid reaction rates in unsaturated porous media. *Chemical Geology*, *421*, 65–80. https://doi.org/10.1016/j.chemgeo.2015.12.005

Hebert, V., Garing, C., Luquot, L., Pezard, P., & Gouze, P. (2015). Multi-scale X-ray tomography analysis of carbonate porosity. *Geological Society, London, Special Publications*, *406*(1), 61–79. https://doi.org/10.1144/sp406.12

Heyman, J., Lester, D. R., Turuban, R., Méheust, Y., & Le Borgne, T. (2020). Stretching and folding sustain microscale chemical gradients in porous media. *Proceedings of the National Academy of Sciences*, *117*(24), 13359–13365. https://doi.org/10.1073/pnas.2002858117

Izumoto, S., Heyman, J., Huisman, J. A., De Vriendt, K., Soulaine, C., Gomez, F., et al. (2023). Enhanced mixing and reaction in converging flows: Theory and pore-scale imaging. *Water Resources Research*, *59*(8), e2023WR034749. https://doi.org/10.1029/2023wr034749

Izumoto, S., Huisman, J. A., Zimmermann, E., Heyman, J., Gomez, F., Tabuteau, H., et al. (2022). Pore-scale mechanisms for spectral induced polarization of calcite precipitation inferred from geo-electrical millifluidics. *Environmental Science & Technology*, *56*(8), 4998–5008. https://doi.org/10.1021/acs.est.1c07742

Izumoto, S., Rousseau, G., Le Borgne, T., & Heyman, J. (2025). Effective reaction kinetics of steady mixing fronts in porous media. *Journal of Fluid Mechanics*, *1013*, A4. https://doi.org/10.1017/jfm.2025.10223

Kaestner, A. (2011). Muhrec—A new tomography reconstructor. *Nuclear Instruments and Methods in Physics Research Section A: Accelerators, Spectrometers, Detectors and Associated Equipment*, *651*(1), 156–160. https://doi.org/10.1016/j.nima.2011.01.129

Kaestner, A., Hartmann, S., Kühne, G., Frei, G., Grünzweig, C., Josic, L., et al. (2011). The ICON beamline–A facility for cold neutron imaging at SINQ. *Nuclear Instruments and Methods in Physics Research Section A: Accelerators, Spectrometers, Detectors and Associated Equipment*, *659*(1), 387–393. https://doi.org/10.1016/j.nima.2011.08.022

Kaestner, A., Lehmann, E., & Stampanoni, M. (2008). Imaging and image processing in porous media research. *Advances in Water Resources*, *31*(9), 1174–1187. https://doi.org/10.1016/j.advwatres.2008.01.022

Kaestner, A., Morgano, M., Hovind, J., & Lehmann, E. (2015). Bimodal imaging using neutrons and X-rays. In *Proceedings of the international symposium on digital industrial radiology and computed tomography*. Retrieved from http://www.ndt.net/events/dir2015/paper/58_kaestner.pdf

Kaestner, A. P., Trtik, P., Zarebanadkouki, M., Kazantsev, D., Snehota, M., Dobson, K. J., & Lehmann, E. H. (2016). Recent developments in neutron imaging with applications for porous media research. *Solid Earth*, *7*(5), 1281–1292. https://doi.org/10.5194/se-7-1281-2016

Kampman, N., Bickle, M., Wigley, M., & Dubacq, B. (2014). Fluid flow and $CO_2$–fluid–mineral interactions during $CO_2$-storage in sedimentary basins. *Chemical Geology*, *369*, 22–50. https://doi.org/10.1016/j.chemgeo.2013.11.012

Kanakiya, S., Adam, L., Esteban, L., Rowe, M. C., & Shane, P. (2017). Dissolution and secondary mineral precipitation in basalts due to reactions with carbonic acid. *Journal of Geophysical Research: Solid Earth*, *122*(6), 4312–4327. https://doi.org/10.1002/2017jb014019

Kang, P. K., Bresciani, E., An, S., & Lee, S. (2019). Potential impact of pore-scale incomplete mixing on biodegradation in aquifers: From batch experiment to field-scale modeling. *Advances in Water Resources*, *123*, 1–11. https://doi.org/10.1016/j.advwatres.2018.10.026

Leaist, D. G., & Noulty, R. A. (1985). Multicomponent diffusion of aqueous sodium carbonate and aqueous sodium bicarbonate. *Canadian Journal of Chemistry*, *63*(8), 2319–2323. https://doi.org/10.1139/v85-383

Liu, C., Liu, Y., Kerisit, S., & Zachara, J. (2015). Pore-scale process coupling and effective surface reaction rates in heterogeneous subsurface materials. *Reviews in Mineralogy and Geochemistry*, *80*(1), 191–216. https://doi.org/10.2138/rmg.2015.80.06

Luhmann, A. J., Tutolo, B. M., Bagley, B. C., Mildner, D. F., Seyfried Jr, W. E., & Saar, M. O. (2017). Permeability, porosity, and mineral surface area changes in basalt cores induced by reactive transport of $CO_2$-rich brine. *Water Resources Research*, *53*(3), 1908–1927. https://doi.org/10.1002/2016wr019216

Mancini, L., Arzilli, F., Polacci, M., & Voltolini, M. (2020). *Recent advancements in X-ray and neutron imaging of dynamic processes in Earth Sciences* (Vol. 8). Frontiers Media SA.

Mathiesen, J., Linga, G., Misztal, M., Renard, F., & Le Borgne, T. (2023). Dynamic fluid connectivity controls solute dispersion in multiphase porous media flow. *Geophysical Research Letters*, *50*(16), e2023GL105233. https://doi.org/10.1029/2023gl105233

Matter, J. M., Takahashi, T., & Goldberg, D. (2007). Experimental evaluation of in situ $CO_2$-water-rock reactions during $CO_2$ injection in basaltic rocks: Implications for geological $CO_2$ sequestration. *Geochemistry, Geophysics, Geosystems*, *8*(2). https://doi.org/10.1029/2006gc001427

Menefee, A. H., Giammar, D. E., & Ellis, B. R. (2018). Permanent $CO_2$ trapping through localized and chemical gradient-driven basalt carbonation. *Environmental Science & Technology*, *52*(15), 8954–8964. https://doi.org/10.1021/acs.est.8b01814

Montes-Hernandez, G., Findling, N., & Renard, F. (2016). Dissolution-precipitation reactions controlling fast formation of dolomite under hydrothermal conditions. *Applied Geochemistry*, *73*, 169–177. https://doi.org/10.1016/j.apgeochem.2016.08.011

Nisbet, H., Buscarnera, G., Carey, J., Detournay, E., Huang, H., Hyman, J., et al. (2024). Carbon mineralization in fractured mafic and ultramafic rocks: A review. *Reviews of Geophysics*, *62*(4), e2023RG000815. https://doi.org/10.1029/2023rg000815

Noiriel, C., & Soulaine, C. (2021). Pore-scale imaging and modelling of reactive flow in evolving porous media: Tracking the dynamics of the fluid–rock interface. *Transport in Porous Media*, *140*(1), 181–213. https://doi.org/10.1007/s11242-021-01613-2

Oelkers, E. H., Gislason, S. R., & Matter, J. (2008). Mineral carbonation of $CO_2$. *Elements*, *4*(5), 333–337. https://doi.org/10.2113/gselements.4.5.333

Oelkers, E. H., & Gislason, S. R. (2023). Carbon capture and storage: From global cycles to global solutions. *Geochemical Perspectives*, *12*(2), 179–180. https://doi.org/10.7185/geochempersp.12.2

Peuble, S., Godard, M., Luquot, L., Andreani, M., Martinez, I., & Gouze, P. (2015). $CO_2$ geological storage in olivine rich basaltic aquifers: New insights from reactive-percolation experiments. *Applied Geochemistry*, *52*, 174–190. https://doi.org/10.1016/j.apgeochem.2014.11.024

Porta, G. M., Riva, M., & Guadagnini, A. (2012). Upscaling solute transport in porous media in the presence of an irreversible bimolecular reaction. *Advances in Water Resources*, *35*, 151–162. https://doi.org/10.1016/j.advwatres.2011.09.004

Postma, T., Bandilla, K., Peters, C., & Celia, M. (2022). Field-scale modeling of $CO_2$ mineral trapping in reactive rocks: A vertically integrated approach. *Water Resources Research*, *58*(1), e2021WR030626. https://doi.org/10.1029/2021wr030626

Putnis, A. (2021). Fluid–mineral interactions: Controlling coupled mechanisms of reaction, mass transfer and deformation. *Journal of Petrology*, *62*(12), egab092. https://doi.org/10.1093/petrology/egab092

Puyguiraud, A., Gouze, P., & Dentz, M. (2021). Pore-scale mixing and the evolution of hydrodynamic dispersion in porous media. *Physical Review Letters*, *126*(16), 164501. https://doi.org/10.1103/physrevlett.126.164501

Ribeiro, A. C., Barros, M. C., Teles, A. S., Valente, A. J., Lobo, V. M., Sobral, A. J., & Esteso, M. (2008). Diffusion coefficients and electrical conductivities for calcium chloride aqueous solutions at 298.15 k and 310.15 k. *Electrochimica Acta*, *54*(2), 192–196. https://doi.org/10.1016/j.electacta.2008.08.011

Rolle, M., & Le Borgne, T. (2019). Mixing and reactive fronts in the subsurface. *Reviews in Mineralogy and Geochemistry*, *85*(1), 111–142. https://doi.org/10.2138/rmg.2018.85.5

Ruiz-Agudo, E., Burgos-Cara, A., Ruiz-Agudo, C., Ibañez-Velasco, A., Cölfen, H., & Rodriguez-Navarro, C. (2017). A non-classical view on calcium oxalate precipitation and the role of citrate. *Nature Communications*, *8*(1), 768. https://doi.org/10.1038/s41467-017-00756-5

Sabo, M. S., & Beckingham, L. E. (2021). Porosity-permeability evolution during simultaneous mineral dissolution and precipitation. *Water Resources Research*, *57*(6), e2020WR029072. https://doi.org/10.1029/2020wr029072

Sanquer, H., Heyman, J., Hanna, K., & Le Borgne, T. (2024). Microscale chaotic mixing as a driver for chemical reactions in porous media. *Environmental Science & Technology*, *58*(20), 8899–8908. https://doi.org/10.1021/acs.est.3c09749

Scanziani, A., Alhosani, A., Lin, Q., Spurin, C., Garfi, G., Blunt, M. J., & Bijeljic, B. (2020). In situ characterization of three-phase flow in mixed-wet porous media using synchrotron imaging. *Water Resources Research*, *56*(9), e2020WR027873. https://doi.org/10.1029/2020wr027873

Shafabakhsh, P. (2024). Time-lapse imaging of reactive mixing inducing carbonate mineralization in basalt cores [Dataset]. https://doi.org/10.11582/2024.00144

Shafabakhsh, P., Cordonnier, B., Pluymakers, A., Le Borgne, T., Mathiesen, J., Linga, G., et al. (2024). 4D neutron imaging of solute transport and fluid flow in sandstone before and after mineral precipitation. *Water Resources Research*, *60*(3), e2023WR036293. https://doi.org/10.1029/2023wr036293

Shafabakhsh, P., Le Borgne, T., Renard, F., & Linga, G. (2024). Resolving pore-scale concentration gradients for transverse mixing and reaction in porous media. *Advances in Water Resources*, *192*, 104791. https://doi.org/10.1016/j.advwatres.2024.104791

Sole-Mari, G., Fernàndez-Garcia, D., Sanchez-Vila, X., & Bolster, D. (2020). Lagrangian modeling of mixing-limited reactive transport in porous media: Multirate interaction by exchange with the mean. *Water Resources Research*, *56*(8), e2019WR026993. https://doi.org/10.1029/2019wr026993

Steefel, C. (2018). *Reactive transport modeling: Applications in subsurface energy and environmental problems*. John Wiley & Sons.

Sun, L., Liu, Y., Cheng, Z., Jiang, L., Lv, P., & Song, Y. (2023). Review on multiscale $CO_2$ mineralization and geological storage: Mechanisms, characterization, modeling, applications and perspectives. *Energy & Fuels*, *37*(19), 14512–14537. https://doi.org/10.1021/acs.energyfuels.3c01830

Tartakovsky, A. M., Redden, G., Lichtner, P. C., Scheibe, T. D., & Meakin, P. (2008). Mixing-induced precipitation: Experimental study and multiscale numerical analysis. *Water Resources Research*, *44*(6). https://doi.org/10.1029/2006wr005725

Tenchine, S., & Gouze, P. (2005). Density contrast effects on tracer dispersion in variable aperture fractures. *Advances in Water Resources*, *28*(3), 273–289. https://doi.org/10.1016/j.advwatres.2004.10.009

Tengattini, A., Lenoir, N., Andò, E., Giroud, B., Atkins, D., Beaucour, J., & Viggiani, G. (2020). NeXT-Grenoble, the Neutron and X-ray tomograph in Grenoble. *Nuclear Instruments and Methods in Physics Research Section A: Accelerators, Spectrometers, Detectors and Associated Equipment*, *968*, 163939. https://doi.org/10.1016/j.nima.2020.163939

Tengattini, A., Lenoir, N., Andò, E., & Viggiani, G. (2021). Neutron imaging for geomechanics: A review. *Geomechanics for Energy and the Environment*, *27*, 100206. https://doi.org/10.1016/j.gete.2020.100206

Tudisco, E., Etxegarai, M., Hall, S. A., Charalampidou, E.-M., Couples, G. D., Lewis, H., et al. (2019). Fast 4-D imaging of fluid flow in rock by high-speed neutron tomography. *Journal of Geophysical Research: Solid Earth*, *124*(4), 3557–3569. https://doi.org/10.1029/2018jb016522

Tutolo, B. M., Luhmann, A. J., Kong, X.-Z., Saar, M. O., & Seyfried Jr, W. E. (2015). $CO_2$ sequestration in feldspar-rich sandstone: Coupled evolution of fluid chemistry, mineral reaction rates, and hydrogeochemical properties. *Geochimica et Cosmochimica Acta*, *160*, 132–154. https://doi.org/10.1016/j.gca.2015.04.002

Valocchi, A. J., Bolster, D., & Werth, C. J. (2019). Mixing-limited reactions in porous media. *Transport in Porous Media*, *130*(1), 157–182. https://doi.org/10.1007/s11242-018-1204-1

Wang, W., Xie, Q., An, S., Bakhshian, S., Kang, Q., Wang, H., et al. (2023). Pore-scale simulation of multiphase flow and reactive transport processes involved in geologic carbon sequestration. *Earth-Science Reviews*, *247*, 104602. https://doi.org/10.1016/j.earscirev.2023.104602

Wennberg, O. P., Rennan, L., & Basquet, R. (2009). Computed tomography scan imaging of natural open fractures in a porous rock; geometry and fluid flow. *Geophysical Prospecting*, *57*(2), 239–249. https://doi.org/10.1111/j.1365-2478.2009.00784.x

Willingham, T. W., Werth, C. J., & Valocchi, A. J. (2008). Evaluation of the effects of porous media structure on mixing-controlled reactions using pore-scale modeling and micromodel experiments. *Environmental Science & Technology*, *42*(9), 3185–3193. https://doi.org/10.1021/es7022835

Xu, R., Li, R., Ma, J., He, D., & Jiang, P. (2017). Effect of mineral dissolution/precipitation and $CO_2$ exsolution on $CO_2$ transport in geological carbon storage. *Accounts of Chemical Research*, *50*(9), 2056–2066. https://doi.org/10.1021/acs.accounts.6b00651

Zhang, P., Wittmann, F., Zhao, T., & Lehmann, E. (2010). Neutron imaging of water penetration into cracked steel reinforced concrete. *Physica B: Condensed Matter*, *405*(7), 1866–1871. https://doi.org/10.1016/j.physb.2010.01.065

Zhang, X., Dou, Z., Hamada, M., de Anna, P., & Jimenez-Martinez, J. (2025). Enhanced reaction kinetics in stationary two-phase flow through porous media. *Environmental Science & Technology*, *59*(2), 1334–1343. https://doi.org/10.1021/acs.est.4c09449

Zhao, C., Xiao, Y., Chu, J., Hu, R., Liu, H., He, X., et al. (2023). Microfluidic experiments of biological $CaCO_3$ precipitation in transverse mixing reactive environments. *Acta Geotechnica*, *18*(10), 5299–5318. https://doi.org/10.1007/s11440-023-01938-w

Ziesche, R. F., Hack, J., Rasha, L., Maier, M., Tan, C., Heenan, T. M., et al. (2022). High-speed 4D neutron computed tomography for quantifying water dynamics in polymer electrolyte fuel cells. *Nature Communications*, *13*(1), 1616. https://doi.org/10.1038/s41467-022-29313-5

Ziesche, R. F., Arlt, T., Finegan, D. P., Heenan, T. M., Tengattini, A., Baum, D., et al. (2020). 4D imaging of lithium-batteries using correlative neutron and X-ray tomography with a virtual unrolling technique. *Nature Communications*, *11*(1), 777. https://doi.org/10.1038/s41467-019-13943-3

Zou, S., & Sun, C. (2020). X-ray microcomputed imaging of wettability characterization for multiphase flow in porous media: A review. *Capillarity*, *3*(3), 36–44. https://doi.org/10.46690/capi.2020.03.01